Analytic Model Predictive Current Control of Grid-Connected Power Conversion System in Battery Energy Storage System

Mingming Zhang, Mian Li, *Member, IEEE*, and Jun Zhang, *Senior Member, IEEE*

***Abstract*—In this article, an analytic model predictive current controller is proposed for the grid-connected power conversion system (PCS) in the battery energy storage system (BESS). This controller is designed to provide the fast and robust dynamic response while maintaining the moderate computational cost, making it suitable for real-time industrial microcontrollers. An accurate discrete-time model of the grid-connected PCS is derived to enable a closed-form solution, and the 3-D current reference tracking problem, incorporating the varying dc-link voltage of the BESS, is formulated as a multiparametric quadratic program. For this optimization problem, the constrained optimal control law is shown to be the accurate orthogonal projection of the unconstrained solution onto the corresponding active voltage constraint. Subsequently, an efficient geometric method is developed to obtain the analytic optimal control in the general case, enabling the online application of MPC with a long prediction horizon for industrial PCS. Moreover, a disturbance observer is combined with the predictive current controller to ensure offset-free tracking and robustness against system uncertainties. Simulation and experimental results on a 20 kVA PCS demonstrate the fast dynamics, low total harmonic distortion, strong robustness, and high computational efficiency of the proposed current controller.**

***Index Terms*—Analytic model predictive current controller (APCC), grid-connected battery energy storage system (BESS), high computational efficiency, long prediction horizon, power conversion system (PCS).**

I. Introduction

With the rapid development of the renewable energy integration, the battery energy storage system (BESS) is getting increasingly important in modern grids. The BESS can provide a wide range of benefits, including fast response to the grid frequency regulation and voltage support, effective smoothing of intermittent energy outputs such as solar and wind, and efficient peak shaving under varying grid loads [1]. Specifically, the required efficient and reliable power conversion between the grid and the BESS is realized by the grid-connected power conversion system (PCS), which not only facilitates the grid voltage support and frequency regulation, but also compensates for the reactive power according to the grid demands [2].

The grid-connected PCS in BESS is typically controlled using a cascaded dual-loop structure under the grid following strategy. The outer loop can either be a voltage control loop (e.g., the dc-link voltage control) or a power control loop (e.g., the reactive power control), and the inner loop controls the current, each adapted to their respective time scales [3]. Therefore, a fast and robust current controller is essential to ensure the optimal performance of the grid-connected system under varying operating conditions. Notably, this control system is a multi-input–multi-output (MIMO) system, and features on the control inputs and the system states are physically constrained by the dc-link voltage supplied by the BESS and the converter hardware limitations. Furthermore, the current controller must contend with various uncertainties, including grid fluctuations, model inaccuracies, and external disturbances [4].

In today's industrial applications, the current controller of the grid-connected PCS is often implemented with the Proportional–Integral (PI) algorithm in the dq-frame, which is commonly combined with a feed-forward term to compensate the cross-coupling effects of the system [5], [6], [7]. Since accurate electrical parameters are required to effectively decouple the dynamics of the grid-connected PCS, a pseudo multivariable current controller based on the pseudoconverter model is proposed to achieve more efficient decoupling capability [8]. Further, Bahrani et al. [9] improved the pseudo multivariable controller and developed an optimization based multivariable PI current controller (OMCC) to enhance the dynamic response as well as ensure the closed-loop stability. Although these PI-based controllers are easy to realize, the dynamic response of PI controller may be slow due to the integral action. Moreover, it is difficult to effectively handle the control saturation and overshoot particularly during the disturbed working conditions.

The Proportional-Resonant (PR) controller designed in the $\alpha\beta$-frame is another widely recognized current controller in the grid-connected PCS, and is renowned for its offset-free tracking performance [10], [11]. However, its sensitivity to parameter variations can degrade control performance and necessitating frequently parameter tuning due to its narrow control bandwidth [12]. Besides, the improved repetitive current

Received 14 May 2024; revised 14 September 2024; accepted 10 November 2024. Date of publication 18 November 2024; date of current version 26 December 2024. This work was supported by the National Natural Science Foundation of China under Grant 52275263 and Grant 62173229. Recommended for publication by Associate Editor B. Mirafzal. *(Corresponding author: Jun Zhang.)*

Mingming Zhang and Mian Li are with the Global Institute of Future Technology, Shanghai Jiao Tong University, Shanghai 200240, China (e-mail: brucechang@sjtu.edu.cn; mianli@sjtu.edu.cn).

Jun Zhang is with the UMich-SJTU Joint Institute, Shanghai Jiao Tong University, Shanghai 200240, China (e-mail: zhangjun12@sjtu.edu.cn).

Color versions of one or more figures in this article are available at https://doi.org/10.1109/TPEL.2024.3501295.

Digital Object Identifier 10.1109/TPEL.2024.3501295

controller in [13] can also effectively eliminate the steady-state tracking errors and minimize the total harmonic distortion (THD) using the internal model principle. Recently, Harnefors [14], [15] proposed an actively damped robust vector current controller (robust VCC) for grid-connected converters, which demonstrates stable and well-performing operations irrespective of the grid strength. Moreover, several robust current controllers based on the robust control theory have been reported in [16], [17], and [18] to enhance system dynamics and fortify resilience against disturbances, but the parameters tuning strategy can be complicated and demand considerable computational resources.

Over the past decades, model predictive controller (MPC) has gained popularity for enhancing the control performance of industrial power converters [19]. MPC is beneficial at managing the MIMO grid-connected PCS by optimizing all variables simultaneously, resulting in enhanced overall performance and coordination. In addition, MPC can explicitly handle system constraints within its optimization framework, ensuring the converter operates safely and efficiently within its physical limits. Furthermore, by incorporating system uncertainties into its prediction model, MPC proactively adjusts control inputs to mitigate disturbances, thus enhancing the system's robustness and reliability [20].

Preindl et al. [21] proposed a model predictive direct current controller with short prediction horizon for high power voltage source inverters, where its control input is the discrete switching signals determined by the converter topology. To reduce the averaged switching frequency and the total demand distortion of the currents, Geyer et al. [22] and Karamanakos et al. [23] proposed a MPC with long horizon by inserting an extrapolation operation between two neighboring switching actions. This way, the controller can predict longer state trajectories while maintaining the same control steps, and thus reduce the computation burden.

To achieve precise current control, Linder and Kennel [24] pioneered the explicit MPC (EMPC) technique for the electrical drives, where a modulator is employed to generate continuous real-valued voltage output. A comprehensive description of the EMPC design for the grid-connected inverter is firstly presented in [25], but the prediction horizon is limited less than three steps to avoid the explosion of critical regions. Nevertheless, EMPC is not suitable for the optimal control problems with high dimension and long prediction horizon since the number of explicit solutions grows exponentially with the problem size and complexity [26].

Actually, the performance of MPC in industrial grid-connected PCS is primarily influenced by the controller structure, computational capability, and the length of the prediction horizon. These factors are usually conflictive in practical applications. Particularly, the MPC with long prediction horizon is beneficial to provide stability and invariance but requires considerable computation resources to solve the Algebraic Riccati Equation [27]. In this article, we aim at developing an analytic MPC with fast dynamic response but at moderate computational cost, such that it can be feasibly implemented in the industrial real-time microcontrollers. The main contributions of this article are as follows:

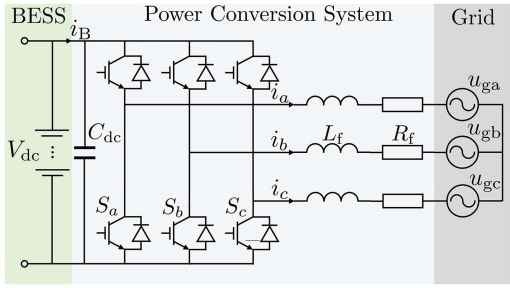

Fig. 1. Topology of the three-phase two-level PCS in the grid-connected BESS.

1) An accurate discrete-time system model is derived for the PCS. The system and input matrices are shown to be the SRM, which reveals the physical nature of the grid-connected PCS and can significantly simplify the derivation of the closed-form optimal control law.
2) The current reference tracking problem incorporating the dc-link voltage variation of the BESS is formulated as a 3-D mp-QP problem, then the optimal control law is only a piecewise function of initial current state within each critical region.
3) Both the constrained and unconstrained optimal control laws in the 2-D current plane for a specific dc-link voltage are derived explicitly. The constrained optimal control is shown to be the geometric orthogonal projection of the unconstrained solution onto the active voltage constraint. Moreover, the obtained results in 2-D case can be directly extended to the original 3-D problem.
4) An analytic model predictive current controller (APCC) with a long prediction horizon is proposed for the grid-connected PCS in general case, which can be feasibly implemented in the low-cost industrial microcontrollers. Only one tuning parameter is required to set the desired closed-loop bandwidth of the proposed current controller.

Experimental results demonstrate that our method achieves satisfactory control performance in a 20 kVA grid-connected PCS of the BESS.

II. Discrete-Time Modeling of Grid-Connected PCS

In this section, we derive an accurate discrete-time model for the grid-connected PCS of the BESS.

A. Continuous-Time Model

The three-phase two-level bidirectional PCS has been widely used nowadays in the grid-connected BESS, as is illustrated in Fig. 1. According to the Kirchhoff's laws, the dynamic equation of the PCS in the natural abc-frame is obtained as

$$\begin{aligned} L_{\mathrm{f}}\frac{di_a}{dt} &= -R_{\mathrm{f}}i_a + u_a - V_{\mathrm{g}}\cos(\theta_{\mathrm{g}}) \\ L_{\mathrm{f}}\frac{di_b}{dt} &= -R_{\mathrm{f}}i_b + u_b - V_{\mathrm{g}}\cos\left(\theta_{\mathrm{g}} + \frac{2\pi}{3}\right) \\ L_{\mathrm{f}}\frac{di_c}{dt} &= -R_{\mathrm{f}}i_b + u_c - V_{\mathrm{g}}\cos\left(\theta_{\mathrm{g}} - \frac{2\pi}{3}\right) \end{aligned} \tag{1}$$

where u_{abc} is the output voltage of the converter, i_{abc} is the converter current, $V_{\rm g}$ is the grid voltage amplitude, and $\theta_{\rm g}$ is the grid phase angle. $L_{\rm f}$ is the filter inductance and $R_{\rm f}$ is the filter resistance. Additionally, the dynamics of the dc-link voltage provided by the BESS is given by

$$C_{\rm dc}\frac{dV_{\rm dc}}{dt} = i_{\rm B} - (S_a i_a + S_b i_b + S_c i_c) \tag{2}$$

where $V_{\rm dc}$ is the dc-link voltage, $i_{\rm B}$ is the current flowing out from the battery, S_{abc} is the switching function, and $C_{\rm dc}$ is the dc-link capacitance.

In discharging mode, the current flows from the BESS to the grid via the PCS, causing a decrease in dc-link voltage $V_{\rm dc}$. Conversely, in charging mode, current flows from the grid to the BESS, resulting in an increase in $V_{\rm dc}$. As is well-known that the dynamics of the dc-link voltage is much slower than those of the converter currents [4], the dc-link voltage $V_{\rm dc}$ can be regarded as quasi-constant during a single current control period.

To simplify the design and analysis of the current controller, the converter is typically controlled in the linear rotationary dq-frame and rather than the original nonlinear stationary abc-frame. Specifically, the variables in (1) are transformed from the abc-frame to the dq-frame with the Clarke and Park transformation $T_{\rm CP}$

$$T_{\rm CP} = \frac{2}{3}\begin{bmatrix} \cos\theta_{\rm g} & \cos\left(\theta_{\rm g}-\frac{2}{3}\pi\right) & \cos\left(\theta_{\rm g}+\frac{2}{3}\pi\right) \\ -\sin\theta_{\rm g} & -\sin\left(\theta_{\rm g}-\frac{2}{3}\pi\right) & -\sin\left(\theta_{\rm g}+\frac{2}{3}\pi\right) \end{bmatrix} \tag{3}$$

and then the continuous-time model of the grid-connected PCS is governed by

$$\frac{d}{dt}\boldsymbol{i} = \boldsymbol{A}_c\boldsymbol{i}(t) + \boldsymbol{B}_c\boldsymbol{u}(t) + \boldsymbol{g}_c \tag{4}$$

where $\boldsymbol{u} = [u_d, u_q]^T$ and $\boldsymbol{i} = [i_d, i_q]^T$ are the voltage and current of the converter, respectively, and

$$\boldsymbol{A}_c = \begin{bmatrix} -\frac{R_{\rm f}}{L_{\rm f}} & \omega_{\rm g} \\ -\omega_{\rm g} & -\frac{R_{\rm f}}{L_{\rm f}} \end{bmatrix},\ \boldsymbol{B}_c = \begin{bmatrix} \frac{1}{L_{\rm f}} & 0 \\ 0 & \frac{1}{L_{\rm f}} \end{bmatrix},\ \boldsymbol{g}_c = \begin{bmatrix} \frac{V_{\rm g}}{L_{\rm f}} \\ 0 \end{bmatrix}. \tag{5}$$

The corresponding dc-link voltage dynamics in the dq-frame becomes

$$C_{\rm dc}\frac{dV_{\rm dc}}{dt} = \frac{3}{2}\left[i_{\rm B} - (S_d i_d + S_q i_q)\right] = \frac{3}{2}\left(\frac{\boldsymbol{u}^T\boldsymbol{i}}{V_{\rm dc}} - \boldsymbol{S}^T\boldsymbol{i}\right) \tag{6}$$

where $\boldsymbol{S} = [S_d, S_q]^T$ is the dq-component of the switching function, and the last equality holds due to the power conservation law.

B. Discrete-Time Model

In engineering practice, the controller is commonly implemented on digital signal processing board, requiring a discrete-time model for both design and analysis purposes. From the continuous-time PCS model (4), the zero-order hold equivalent discrete-time model, with a sampling time T_s, is derived as follows:

$$\boldsymbol{i}(k+1) = \boldsymbol{F}\boldsymbol{i}(k) + \boldsymbol{B}\boldsymbol{u}(k) + \boldsymbol{g} \tag{7}$$

where

$$\begin{aligned} \boldsymbol{F} &= e^{\boldsymbol{A}_c T_s}, \quad \boldsymbol{B} = \boldsymbol{A}_c^{-1}(e^{\boldsymbol{A}_c T_s} - \boldsymbol{I})\boldsymbol{B}_c \\ \boldsymbol{g} &= \boldsymbol{A}_c^{-1}(e^{\boldsymbol{A}_c T_s} - \boldsymbol{I})\boldsymbol{g}_c. \end{aligned} \tag{8}$$

Moreover, we can show that the system matrix F can be written as

$$\boldsymbol{F} = e^{-\frac{R_{\rm f}T_s}{L_{\rm f}}}\begin{bmatrix} \cos\omega_{\rm g}T_s & \sin\omega_{\rm g}T_s \\ -\sin\omega_{\rm g}T_s & \cos\omega_{\rm g}T_s \end{bmatrix} = s_F R(-\omega_{\rm g}T_s) \tag{9}$$

where $s_F < 1$, and $R(\cdot)$ is the rotation matrix. Then

$$\boldsymbol{F}^T\boldsymbol{F} = s_F^2\mathbf{I}, \quad \boldsymbol{F} + \boldsymbol{F}^T = 2s_F\cos\omega_{\rm g}T_s\mathbf{I}. \tag{10}$$

We can also express the input matrix as $\boldsymbol{B} = s_B R(\theta_B)$, where

$$s_B = \sqrt{\frac{e^{-2R_{\rm f}/L_{\rm f}T_s} - 2e^{-R_{\rm f}/L_{\rm f}T_s}\cos\omega_{\rm g}T_s + 1}{R_{\rm f}^2 + L_{\rm f}^2\omega_{\rm g}^2}} \tag{11}$$

and

$$\theta_B = \tan^{-1}\frac{e^{-\frac{R_{\rm f}T_s}{L_{\rm f}}}(L_{\rm f}\omega_{\rm g}\cos\omega_{\rm g}T_s + R_{\rm f}\omega_{\rm g}\sin\omega_{\rm g}T_s) - L_{\rm f}\omega_{\rm g}}{e^{-\frac{R_{\rm f}T_s}{L_{\rm f}}}(L_{\rm f}\omega_{\rm g}\cos\omega_{\rm g}T_s - R_{\rm f}\omega_{\rm g}\sin\omega_{\rm g}T_s) + R_{\rm f}}. \tag{12}$$

Remark 1: The system matrix $\boldsymbol{F}$ and the input matrix $\boldsymbol{B}$ can be understood each as a 2×2 rotation matrix multiplied by a scaling factor. Generally, these 2×2 scaling rotation matrices (SRM) form a field. It is straightforward to show that the sum and product of two such matrices are still SRM.

At steady-state, it is obtained that

$$\bar{\boldsymbol{i}} = \boldsymbol{F}\bar{\boldsymbol{i}} + \boldsymbol{B}\bar{\boldsymbol{u}} + \boldsymbol{g} \tag{13}$$

which yields $\bar{\boldsymbol{u}} = \boldsymbol{B}^{-1}[(\boldsymbol{I}-\boldsymbol{F})\bar{\boldsymbol{i}} - \boldsymbol{g}]$. Subtracting (13) from (7), we have

$$(\boldsymbol{i}_{k+1} - \bar{\boldsymbol{i}}) = \boldsymbol{F}(\boldsymbol{i}_k - \bar{\boldsymbol{i}}) + \boldsymbol{B}(\boldsymbol{u}_k - \bar{\boldsymbol{u}}). \tag{14}$$

Now, we denote $\boldsymbol{x}_k = \boldsymbol{i}_k - \bar{\boldsymbol{i}}$, $\boldsymbol{v}_k = \boldsymbol{u}_k - \bar{\boldsymbol{u}}$, then the system model of the grid-connected PCS can be represented in the form of $\boldsymbol{x}$ and $\boldsymbol{v}$ as follows:

$$\boldsymbol{x}_{k+1} = \boldsymbol{F}\boldsymbol{x}_k + \boldsymbol{B}\boldsymbol{v}_k \tag{15}$$

and (15) also serves as the predictive model for MPC design.

III. Current Reference Tracking Problem Formulation

In this section, we first investigate the physical constraints on the voltage control inputs and system states. Then, we formulate the current reference tracking problem of the grid-connected PCS within the MPC framework, and reveal its equivalence to the multiparametric quadratic problem.

A. Constraints

The voltage control inputs and system current states of the grid-connected PCS in the BESS are primarily limited by the hardware drives, e.g., the duration capabilities of the switches and the dc-link voltage of the BESS. It is essential to accurately describe these constraints to enable the MPC to utilize

the system boundaries effectively and achieve superior control performance.

1) Constraints on the Output Voltage: For the three-phase two-level converter topology, we employ the Space Vector PWM modulation technique in this article to improve the utilization efficiency of the dc-link voltage provided by the BESS. Then, the original output voltage of the PCS in the stationary $\alpha\beta$-frame is constrained by a voltage hexagon represented by the set of linear inequalities $\boldsymbol{A}_u[u_\alpha, u_\beta]^T \le \boldsymbol{b}_u$, where $\boldsymbol{A}_u \in \mathbb{R}^{6\times 2}$ and its mth row is given by

$$\boldsymbol{A}_u^m = \left[\cos\frac{2k+1}{6}\pi, \quad \sin\frac{2k+1}{6}\pi\right], \quad m = 0, \ldots, 5 \tag{16}$$

and $\boldsymbol{b}_u = \frac{\sqrt{3}}{2} b\mathbf{1}$, $b = \frac{2}{3}V_{\text{dc}}$. It means that the size of the voltage hexagon is determined by the dc-link voltage V_{dc} supplied by the BESS and varies during the charging or discharging processes.

Further, given the grid phase angle θ_{g}, the output voltage of the PCS in the rotating dq-frame is constrained by the rotating hexagon $\boldsymbol{A}_u R(\theta_{\text{g}})[u_d, u_q]^T \le \boldsymbol{b}_u$, and the constraints on the kth control voltage are given by

$$\boldsymbol{A}_u R(\theta_{\text{g}} + k\omega_{\text{g}} T_s)\boldsymbol{u}_k \le \boldsymbol{b}_u, \quad k = 0, \ldots, N_p - 1. \tag{17}$$

Equation (17) shows that the two consecutive voltage hexagons differ by a rotating angle $\omega_{\text{g}} T_s$. Letting $\boldsymbol{A}_v^k = \boldsymbol{A}_u R(\theta_{\text{g}} + k\omega_{\text{g}} T_s)$ and substituting it into (17), we have

$$\boldsymbol{A}_v^k \boldsymbol{v}_k \le \boldsymbol{b}_u - \boldsymbol{A}_v^k \bar{\boldsymbol{u}} \triangleq \boldsymbol{b}_v^k. \tag{18}$$

Note that each control $\boldsymbol{v}_k$ is subject to $N_u = 6$ inequalities, resulting in a total $6N_p$ constraints for all control inputs.

2) Constraints on the Converter Current: To ensure the safe operation of the grid-connected BESS, the permitted converter current is usually constrained by a current circle $\|\boldsymbol{i}_s\|_2 \le I_{\max}$ and can be approximated by an N_i-polygon: $\boldsymbol{A}_i \boldsymbol{i}_s \le \boldsymbol{b}_i$, $\boldsymbol{A}_i \in \mathbb{R}^{N_i \times 2}$. The larger the N_i is chosen, the approximation is more close to the current circle. Furthermore, we have

$$\boldsymbol{A}_i \boldsymbol{x}_k = \boldsymbol{A}_i \boldsymbol{i}_k - \boldsymbol{A}_i \bar{\boldsymbol{i}} \le \boldsymbol{b}_i - \boldsymbol{A}_i \bar{\boldsymbol{i}} \triangleq \boldsymbol{b}_x. \tag{19}$$

Then, the system state of the grid-connected PCS at the kth step is obtained iteratively as

$$\boldsymbol{x}_k = \boldsymbol{F}^k \boldsymbol{x}_0 + \boldsymbol{F}^{k-1}\boldsymbol{B}\boldsymbol{v}_0 + \cdots + \boldsymbol{B}\boldsymbol{v}_{k-1}. \tag{20}$$

In matrix form, the current constraint is given by

$$\underbrace{\begin{bmatrix} \boldsymbol{x}_1 \\ \boldsymbol{x}_2 \\ \boldsymbol{x}_3 \\ \vdots \end{bmatrix}}_{\mathcal{X}} = \underbrace{\begin{bmatrix} \boldsymbol{F} \\ \boldsymbol{F}^2 \\ \boldsymbol{F}^3 \\ \vdots \end{bmatrix}}_{\mathcal{S}_x} \boldsymbol{x}_0 + \underbrace{\begin{bmatrix} \boldsymbol{B} & \boldsymbol{0} & \boldsymbol{0} & \\ \boldsymbol{F}\boldsymbol{B} & \boldsymbol{B} & \boldsymbol{0} & \\ \boldsymbol{F}^2\boldsymbol{B} & \boldsymbol{F}\boldsymbol{B} & \boldsymbol{B} & \\ & & & \ddots \end{bmatrix}}_{\mathcal{S}_u} \underbrace{\begin{bmatrix} \boldsymbol{v}_0 \\ \boldsymbol{v}_1 \\ \boldsymbol{v}_2 \\ \vdots \end{bmatrix}}_{\boldsymbol{V}_0} \tag{21}$$

which can be compactly written as

$$(\boldsymbol{I}_{N_p} \otimes \boldsymbol{A}_i)\mathcal{S}_u \boldsymbol{V}_0 \le -(\boldsymbol{I}_{N_p} \otimes \boldsymbol{A}_i)\mathcal{S}_x \boldsymbol{x}_0 + \mathbf{1}_{N_p} \otimes \boldsymbol{b}_x. \tag{22}$$

3) Combination of These Two Constraints: Combining both the voltage control input constraints (18) and the converter current state constraints (22) of the PCS together, we have

$$\boldsymbol{G}\boldsymbol{V}_0 \le \boldsymbol{E}\boldsymbol{x}_0 + \boldsymbol{w} \tag{23}$$

where

$$\boldsymbol{G} = \begin{bmatrix} \mathcal{A}_v \\ \boldsymbol{0} \\ (\boldsymbol{I}_{N_p} \otimes \boldsymbol{A}_i)\mathcal{S}_u \end{bmatrix}, \quad \boldsymbol{E} = \begin{bmatrix} \boldsymbol{0} \\ -\boldsymbol{A}_i \\ -(\boldsymbol{I}_{N_p} \otimes \boldsymbol{A}_i)\mathcal{S}_x \end{bmatrix}$$
$$\boldsymbol{w} = \begin{bmatrix} \mathbf{1}_{N_p} \otimes \boldsymbol{b}_u - \mathcal{A}_v(\mathbf{1}_{N_p} \otimes \bar{\boldsymbol{u}}) \\ \boldsymbol{b}_x \\ \mathbf{1}_{N_p} \otimes \boldsymbol{b}_x \end{bmatrix}. \tag{24}$$

B. Current Reference Tracking Problem Formulation

Now, we proceed to formulate the current reference tracking problem of the grid-connected PCS within the MPC scheme. Typically, the cost function is chosen as the sum of the current tracking error and the penalty associated with the output voltage of the PCS. Mathematically, it is given by

$$J_0 = \frac{1}{2}\sum_{k=1}^{N_p} \boldsymbol{x}_k^T Q \boldsymbol{x}_k + \frac{1}{2}\sum_{k=0}^{N_p-1} \boldsymbol{v}_k^T R \boldsymbol{v}_k. \tag{25}$$

Without loss of generality, letting $Q = 1/s_B^2 \boldsymbol{I}$ and $R = r\boldsymbol{I}$, we have

$$\begin{aligned} J_0 &= \frac{1}{2s_B^2}\mathcal{X}^T\mathcal{X} + \frac{r}{2}\boldsymbol{V}_0^T\boldsymbol{V}_0 \\ &= \frac{1}{2s_B^2}(\mathcal{S}_x\boldsymbol{x}_0 + \mathcal{S}_u\boldsymbol{V}_0)^T(\mathcal{S}_x\boldsymbol{x}_0 + \mathcal{S}_u\boldsymbol{V}_0) + \frac{r}{2}\boldsymbol{V}_0^T\boldsymbol{V}_0 \\ &= \frac{1}{2}\boldsymbol{V}_0^T H \boldsymbol{V}_0 + \boldsymbol{x}_0^T M \boldsymbol{V}_0 + \frac{1}{2}\boldsymbol{x}_0^T Y \boldsymbol{x}_0 \end{aligned} \tag{26}$$

where $H = \frac{1}{s_B^2}\mathcal{S}_u^T\mathcal{S}_u + r\boldsymbol{I}$, $M = \frac{1}{s_B^2}\mathcal{S}_x^T\mathcal{S}_u$, and $Y = \frac{1}{s_B^2}\mathcal{S}_x^T\mathcal{S}_x$.

Combining the discrete-time system model (15), the constraints on both the voltage and currents (23), and the cost function (26), the current reference tracking problem of the grid-connected PCS is formulated as follows:

$$\begin{aligned} \min_{\boldsymbol{V}_0} \quad & J_0 = \frac{1}{2}\begin{bmatrix} \boldsymbol{V}_0^T & \boldsymbol{x}_0^T \end{bmatrix}\begin{bmatrix} H & M^T \\ M & Y \end{bmatrix}\begin{bmatrix} \boldsymbol{V}_0 \\ \boldsymbol{x}_0 \end{bmatrix} \\ \text{s.t.} \quad & \boldsymbol{G}\boldsymbol{V}_0 \le \boldsymbol{E}\boldsymbol{x}_0 + \boldsymbol{w} \\ & \boldsymbol{x}_0 = \boldsymbol{i}(0) - \bar{\boldsymbol{i}}. \end{aligned} \tag{27}$$

It is noted that the MPC problem formulation given in (27) can be transformed into a multiparametric quadratic problem (mp-QP) [28] by letting $\boldsymbol{z} = \boldsymbol{V}_0 + H^{-1}M^T\boldsymbol{x}_0$. Although the software tool developed in [29] is available to solve the mp-QP with short horizon, we aim to propose an efficient method such that our MPC design is applicable to general scenarios featuring a long prediction horizon.

IV. Design and Analysis of APCC

In this section, we investigate the optimal control laws of the current reference tracking problem for the grid-connected PCS. We first study the critical region partitions determined by different combination of active constraints. Subsequently, we explicitly derive the unconstrained and constrained optimal control laws of the MPC, respectively. Then, we establish the geometric

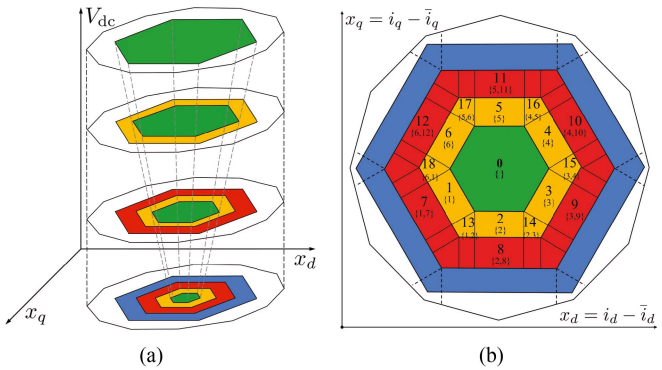

Fig. 2. Critical region partitions. (a) 3-D critical regions with varying dc-link voltage of BESS. (b) 2-D critical regions slide for a specific dc-link voltage.

relationship between the unconstrained and constrained laws, and propose an efficient method to obtain the analytic solution in general case. Finally, we propose an offset-free analytic predictive current controller with long prediction horizon.

For convenience, we primarily elucidate the design and analysis when $N_p = 3$, and demonstrate that the theoretical results obtained there can be readily extended to the general scenario with the prediction horizon $N_p > 3$.

A. Critical Region Partitions

Since the current reference tracking problem formulated in Section III is equivalent to an mp-QP, the optimal control law of the MPC $\boldsymbol{v}_0^*$ can be represented as a piecewise affine function of $\boldsymbol{x}_0$ in each critical region. Specifically, these critical regions are the finite polyhedral partitions of the feasible domain of the problem (27), whose boundaries are determined by combining the primal and dual conditions of the active constraints.

Following this approach, we can obtain the 3-D critical regions of the predictive current control problem, as depicted in Fig. 2(a). The vertical axis labeled as V_{dc} corresponds to the varying dc-link voltage of the BESS, and each horizontal slide of the prism represent the critical region on the current plane associated with a specific V_{dc}. It can be shown that each 2-D slide of the 3-D critical region has the same $\mathcal{CR}$ structure except that the hexagon size varies with the dc-link voltage of the BESS. Moreover, since the dc-link voltage of the BESS exhibits much slower dynamics compared to the converter current, the current controller can be firstly designed in the 2-D case with a fixed V_{dc}, and then directly extended to the original 3-D problem by the gain scheduling technique [30].

For the 2-D critical region partition illustrated in Fig. 2(b), the bracketed number i in each critical region $\mathcal{CR}$ corresponds to the indices of the active constraints. For example, no constraints are active in $\mathcal{CR}_0$. The first control constraint corresponding to $\boldsymbol{v}_0(1)$ is active in $\mathcal{CR}_1$. Two neighboring control constraints with respect to $\boldsymbol{v}_0(1)$ and $\boldsymbol{v}_0(2)$ are simultaneous active in $\mathcal{CR}_{13}$. Moreover, two consecutive control constraints on $\boldsymbol{v}_0(1)$ and $\boldsymbol{v}_1(1)$ are active in $\mathcal{CR}_7$, where the numerical difference between the two indices is 6, which is due to the fact that each control $\boldsymbol{v}_k$ in the control sequence $\boldsymbol{V}$ is subject to $N_u = 6$ inequalities.

Due to the complexity of the derivation of the critical regions, we have omitted the detailed procedure in this paper. Instead, we summarize the key properties associated with these critical regions on the converter current plane as follows.

1) The innermost regular hexagon corresponds to the unconstrained optimal control problem, and its boundary is determined by the first active control $\boldsymbol{v}_0^*$ of PCS. The outermost regular polygon is determined by the constraint on the initial converter current state $\boldsymbol{x}_0$.
2) The rectangular region within the kth hexagon ring corresponds to k consecutive active constraints on control inputs. The active constraints in the wedge region within the kth hexagon ring are a combination of those from its two neighboring rectangular regions.
3) For each rectangular region within the kth hexagon ring, the inner edge is determined by the dual condition of the $(k-1)$th active control $\boldsymbol{v}_{k-1}$, the outer edge is determined by the primal condition of $\boldsymbol{v}_k$, and the edges orthogonal to the hexagon boundary are determined by the primal condition of $\boldsymbol{v}_{k-1}$.

B. Unconstrained Optimal Control Law

Now, we derive the optimal control law when the grid-connected PCS is unconstrained, which means neither the voltage constraints nor the current constraints are active. In this case, the optimal control sequence $\boldsymbol{V}_0^*$ is obtained directly by letting $\partial J_0/\partial \boldsymbol{V}_0 = 0$, and we have

$$\boldsymbol{V}_0^* = -H^{-1}M^T\boldsymbol{x}_0 \triangleq \boldsymbol{V}_{\text{unc}} \tag{28}$$

where H^{-1} is given in (30) shown at the bottom of the next page, and $d_{H3} = (r+1)^3 + r^2 s_F^4 + 2r^2 s_F^2 + 2r s_F^2$ is the square root of the determinant of H. Owing to the commutative properties of the SRM $\boldsymbol{F}$ and $\boldsymbol{B}$, we can easily calculate the optimized control sequence $\boldsymbol{V}_{\text{unc}}$ in elementwise as

$$\begin{aligned}\boldsymbol{V}_{\text{unc}} &= \begin{bmatrix}\boldsymbol{v}_0^* \\ \boldsymbol{v}_1^* \\ \boldsymbol{v}_2^*\end{bmatrix} = \frac{-1}{s_B d_{H3}} \begin{bmatrix} p_1 s_F R(-\omega_{\text{g}} T_s) \\ p_2 s_F^2 R(-2\omega_{\text{g}} T_s) \\ p_3 s_F^3 R(-3\omega_{\text{g}} T_s)\end{bmatrix} R(-\theta_B)\boldsymbol{x}_0 \\ &= \frac{-s_F}{s_B d_{H3}} \begin{bmatrix} (r^2 s_F^4 + r^2 s_F^2 + 2r s_F^2 + (r+1)^2) R(-\omega_{\text{g}} T_s) \\ (r^2 s_F^3 + r^2 s_F + r s_F) R(-2\omega_{\text{g}} T_s) \\ r^2 s_F^2 R(-3\omega_{\text{g}} T_s)\end{bmatrix} \\ &\quad \times R(-\theta_B)\boldsymbol{x}_0. \end{aligned} \tag{29}$$

According to the receding horizon policy of MPC, only the first control element of $\boldsymbol{V}_{\text{unc}}$, denoted as $\boldsymbol{v}_{\text{unc}}$, is applied to drive the grid-connected PCS

C. Constrained Optimal Control Law

In practice, there usually exist working conditions, where the voltage constraints and the current constraints of the PCS are active, e.g., the grid-connected BESS operates under the charging or discharging conditions with large grid power commands. As shown in Section IV-A, the regular hexagon determined by the control input $\boldsymbol{v}_k^*$ expands as k increases, which means the control constraint at $\boldsymbol{v}_k^*$ will be active only when the earlier $\boldsymbol{v}_{k-1}^*$ is active. In other words, the first control constraint at $\boldsymbol{v}_0^*$ will

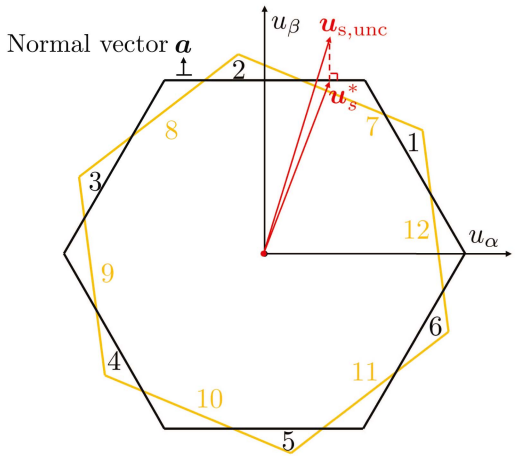

Fig. 3. Constrained optimal solution of the predictive current controller. The black hexagon is the first voltage constraint, and the orange hexagon is the second voltage constraint differed by a rotating angle $\omega_g T_s$. The constrained optimal control law is the orthogonal projection of the unconstrained solution on the active voltage constraint.

become active initially, followed by the second constraint, and so forth.

1) One Active Constraint: Now, we consider the case when only one particular control constraint on $\boldsymbol{v}_0^*$ is active. For example, the critical region $\mathcal{CR}_2$ illustrated in Fig. 2 has one active voltage constraint indexed by the bracketed number 2.

Suppose the voltage control input of the grid-connected PCS is active at the time instant $k=0$, that is $\boldsymbol{v}_0^*$ is located at one edge in Fig. 3. Mathematically, we have $\boldsymbol{G}_A \boldsymbol{V}_0^* - \boldsymbol{b}_0 = 0$, where

$$\begin{aligned} &\boldsymbol{G}_A = \begin{bmatrix} \boldsymbol{a}^T & \mathbf{0} & \mathbf{0} \end{bmatrix}, \boldsymbol{b}_0 = \frac{\sqrt{3}}{2} b - \boldsymbol{a}^T R(\theta_g) \bar{\boldsymbol{u}} \\ &\boldsymbol{a}^T = \begin{bmatrix} \cos\frac{2m+1}{6}\pi & \sin\frac{2m+1}{6}\pi \end{bmatrix} R(\theta_g), \text{ for some } 0 \le m \le 5. \end{aligned} \tag{31}$$

Actually, $\boldsymbol{a}^T$ is the normal vector of the active voltage edge.

To obtain the optimum of the constrained optimization problem, we construct a Lagrange function L_1 as

$$L_1 = J_0 + \lambda(\boldsymbol{G}_A \boldsymbol{V}_0 - b) \tag{32}$$

where $\lambda > 0$ is the Lagrange multiplier. By letting $\partial L_1 / \partial \boldsymbol{V}_0 = 0$, the optimizer of the control problem with one constraint is obtained as

$$\boldsymbol{V}_0^* = -H^{-1} M^T \boldsymbol{x}_0 - \lambda H^{-1} \boldsymbol{G}_A^T = \boldsymbol{V}_{\mathrm{unc}} - \lambda H^{-1} \boldsymbol{G}_A^T. \tag{33}$$

Note that the first term in (33) is precisely the unconstrained optimal solution (28), and the second term is the modification due to the active constraint.

Since the MPC only applies the first control element $\boldsymbol{v}_0^*$ in the optimized control sequence, we focus on the properties of $\boldsymbol{v}_0^*$ and $\boldsymbol{v}_{\mathrm{unc}}$. From (33), we have

$$\boldsymbol{v}_0^* = \boldsymbol{v}_{\mathrm{unc}} - \lambda \underbrace{\begin{bmatrix} \boldsymbol{I} & \mathbf{0} & \mathbf{0} \end{bmatrix} H^{-1} \begin{bmatrix} \boldsymbol{a}^T & \mathbf{0} & \mathbf{0} \end{bmatrix}^T}_{\boldsymbol{a}_p} \tag{34}$$

where the vector $\boldsymbol{a}_p$ determines the direction of the modification. To obtain $\boldsymbol{a}_p$, we only need the first 2×2 submatrix of H^{-1}, which turns out to be a scaled identity matrix $\frac{(r+1)^2 + r s_F^2}{d_{H3}} \boldsymbol{I}$ according to (30). Consequently, the normal vector of the active voltage constraint $\boldsymbol{a}$ and the modification vector $\boldsymbol{a}_p$ satisfies

$$\boldsymbol{a}_p = \frac{(r+1)^2 + r s_F^2}{d_{H3}} \boldsymbol{a} \tag{35}$$

which means that $\boldsymbol{a}_p$ is linearly dependent with $\boldsymbol{a}$, i.e., the direction of the modification term is vertical to the active control constraint.

Therefore, for the problem with only one active constraint, we only need to calculate the unconstrained optimal solution and then perform an orthogonal projection onto the active voltage constraint to obtain the feasible optimal control, as depicted in Fig. 3.[1]

2) Two Active Constraints: Subsequently, we consider the case when two particular voltage constraints of the PCS are active. For instance, the critical region $\mathcal{CR}_8$ in Fig. 2 has two active voltage constraints indexed by the bracketed number 2,8, which is essentially an extension of the critical region $\mathcal{CR}_2$ with only one constraint. In other words, this region indicates that one control constraint is active at the current time instant ($k=0$), and still active at the next time instant ($k=1$), except that their normal vectors differ by a rotating angle $\omega_g T_s$.

Here, we provide a detailed physical explanation of this type of critical region. When the initial current tracking error is far away from the origin, driving the error to converge to zero within one sampling period T_s requires the grid-connected PCS output a large voltage $\boldsymbol{u}_1$ along the correct direction. However, the amplitude of the PCS voltage is limited by the dc-link voltage of the BESS. Consequently, to achieve the same control performance as with $\boldsymbol{u}_1$, the grid-connected PCS can only apply a feasible small $\boldsymbol{u}_2$ in two consecutive sampling periods along this direction, i.e., $\boldsymbol{u}_1 T_s \approx 2\boldsymbol{u}_2 T_s$.

Note that there is another type of critical region with two active voltage constraints, e.g., the wedge region $\mathcal{CR}_{13}$, which corresponds to the first and second voltage constraints are active simultaneously. Since the output voltage of the grid-connected PCS has only two degrees of freedom in the dq-frame, the

[1]Fig. 3 demonstrates the geometric relationship between the unconstrained and constrained optimal solutions in the $\alpha\beta$-frame for intuitive illustration. The validity of this geometric projection is ensured by the linear transformation $\boldsymbol{u} = \boldsymbol{v} + \bar{\boldsymbol{u}}$, followed by the subsequent rotation from $\boldsymbol{u}$ to $\boldsymbol{u}_s$ around the origin.

$$H^{-1} = \frac{1}{d_{H3}} \begin{bmatrix} ((r+1)^2 + r s_F^2)\boldsymbol{I} & -(r+1+r s_F^2)\boldsymbol{F}^T & -r(\boldsymbol{F}^T)^2 \\ -(r+1+r s_F^2)\boldsymbol{F} & ((r+1)^2 + r s_F^4 + r s_F^2 + s_F^2)\boldsymbol{I} & -(r+1)\boldsymbol{F}^T \\ -r\boldsymbol{F}^2 & -(r+1)\boldsymbol{F} & ((r+1)^2 + r s_F^4 + 2r s_F^2 + s_F^2)\boldsymbol{I} \end{bmatrix} \tag{30}$$

optimal control within this region can only lie at the vertex of the corresponding two edges of the voltage hexagon.

Thus, we only need to investigate the critical regions as illustrated by $\mathcal{CR}_8$. Suppose that these two voltage constraints satisfy $\boldsymbol{G}_A\boldsymbol{V}_0^* - b_0 = 0$, where

$$\begin{aligned}
\boldsymbol{G}_A &= \begin{bmatrix} \boldsymbol{a}^T & 0 & 0 \\ 0 & \boldsymbol{a}^T R(\omega_{\mathrm{g}} T_s) & 0 \end{bmatrix}, \\
\boldsymbol{b}_0 &= \begin{bmatrix} \frac{\sqrt{3}}{2} b - \boldsymbol{a}^T R(\theta_{\mathrm{g}}) \bar{\boldsymbol{u}} \\ \frac{\sqrt{3}}{2} b - \boldsymbol{a}^T R(\theta_{\mathrm{g}} + \omega_{\mathrm{g}} T_s) \bar{\boldsymbol{u}} \end{bmatrix} \\
\boldsymbol{a}^T &= \left[\cos \tfrac{2m+1}{6}\pi \quad \sin \tfrac{2m+1}{6}\pi\right] R(\theta_{\mathrm{g}}), \text{ for some } 0 \le m \le 5
\end{aligned} \tag{36}$$

and the rotation matrix $R(\omega_{\mathrm{g}} T_s)$ represents the physical fact that the voltage hexagon rotates with the angle $\omega_{\mathrm{g}} T_s$ during one predictive step.

To obtain the optimum of the constrained optimization problem with two active control constraints, we again construct a Lagrange function L_2 as

$$L_2 = J_0 + \boldsymbol{\lambda}(\boldsymbol{G}_A\boldsymbol{V}_0 - b) = J_0 + \begin{bmatrix} \lambda_1 & \lambda_2 \end{bmatrix} (\boldsymbol{G}_A\boldsymbol{V}_0 - b_0) \tag{37}$$

where the positive λ_1 and λ_2 are the Lagrange multipliers.

Letting $\partial L_2 / \partial \boldsymbol{V}_0 = 0$, we have

$$H\boldsymbol{V}_0^* + M^T \boldsymbol{x}_0 + \boldsymbol{G}_A^T \boldsymbol{\lambda}^T = 0. \tag{38}$$

Thus, the optimized control sequence with two active constraints is obtained as

$$\begin{aligned}
\boldsymbol{V}_0^* &= -H^{-1} M^T \boldsymbol{x}_0 - H^{-1} \boldsymbol{G}_A^T \boldsymbol{\lambda}^T \\
&= \boldsymbol{V}_{\text{unc}} - H^{-1} \boldsymbol{G}_A^T \boldsymbol{\lambda}^T.
\end{aligned} \tag{39}$$

where the first term in (39) is again the unconstrained optimal solution, and the second term is the modification due to the constraint. Similarly, we investigate the relationship between the first optimal control input $\boldsymbol{v}_0^*$ and the unconstrained solution $\boldsymbol{v}_{\text{unc}}$. From (39), we have

$$\begin{aligned}
\boldsymbol{v}_0^* = \boldsymbol{v}_{\text{unc}} &- \lambda_1 \begin{bmatrix} \boldsymbol{I} & \boldsymbol{0} & \boldsymbol{0} \end{bmatrix} H^{-1} \begin{bmatrix} \boldsymbol{a}^T & \boldsymbol{0} & \boldsymbol{0} \end{bmatrix}^T \\
&- \lambda_2 \begin{bmatrix} \boldsymbol{I} & \boldsymbol{0} & \boldsymbol{0} \end{bmatrix} H^{-1} R(-\omega_{\mathrm{g}} T_s) \begin{bmatrix} \boldsymbol{0} & \boldsymbol{a}^T & \boldsymbol{0} \end{bmatrix}^T.
\end{aligned} \tag{40}$$

Moreover, we know from (30) that the second 2×2 submatrix of H^{-1} is the scaling rotation matrix

$$(H^{-1})_{12} = -\frac{r + 1 + r s_F^2}{d_{H3}} \boldsymbol{F}^T = -\frac{r + 1 + r s_F^2}{d_{H3}} s_F R(\omega_{\mathrm{g}} T_s) \boldsymbol{I}. \tag{41}$$

Then, the optimizer $\boldsymbol{v}_0^*$ is obtained as

$$\begin{aligned}
\boldsymbol{v}_0^* &= \boldsymbol{v}_{\text{unc}} - \lambda_1 \frac{(r+1)^2 + r s_F^2}{d_{H3}} \boldsymbol{a} \\
&\quad + \lambda_2 \frac{r + 1 + r s_F^2}{d_{H3}} s_F R(\omega_{\mathrm{g}} T_s) R(-\omega_{\mathrm{g}} T_s) \boldsymbol{a} \\
&= \boldsymbol{v}_{\text{unc}} + c_\lambda \boldsymbol{a}
\end{aligned} \tag{42}$$

which indicates that the modification term $c_\lambda \boldsymbol{a}$ is also vertical to the first active constraint. Thus, the constrained optimal control is again the accurate projection of the unconstrained optimal control onto the active boundary in the voltage plane of the PCS, as shown in Fig. 3.

3) Optimal Solution in General N_p Case: When the prediction step $N_p \ge 3$, we can proceed these analysis procedure for the cases with N_A $(3 \le N_A \le N_p)$ active constraints. When $N_p \ge 3$, the inverse of the matrix H_{N_p} can be calculated as

$$H_{N_p}^{-1} = \frac{1}{d_{H,N_p}} \begin{bmatrix} l_{11}\boldsymbol{I} & l_{12}\boldsymbol{F}^T & \cdots & l_{1,N_p}(\boldsymbol{F}^T)^{N_p-1} \\ l_{21}\boldsymbol{F} & l_{22}\boldsymbol{I} & \cdots & \\ \vdots & & \ddots & \vdots \\ l_{N_p,1}\boldsymbol{F}^{N_p-1} & \cdots & \cdots & l_{N_p,N_p}\boldsymbol{I} \end{bmatrix} \tag{43}$$

where d_{H,N_p} is the determinant, and $l_{i,j}$ is the corresponding coefficients. It shows that the elements in the diagonal line of $H_{N_p}^{-1}$ are scaled identity matrices, and the elements $l_{i,j}$ and $l_{j,i}$ conjugate with each other.

Since we are only interested in the first control element of the optimization sequence, we focus on the first row of $H_{N_p}^{-1}$ which is given by

$$\frac{1}{d_{H,N_p}} \begin{bmatrix} l_{11}\boldsymbol{I}, & l_{21}\boldsymbol{F}^T, & l_{31}(\boldsymbol{F}^T)^2, & \cdots \end{bmatrix} \tag{44}$$

i.e.,

$$\frac{1}{d_{H,N_p}} \begin{bmatrix} l_{11}\boldsymbol{I}, & l_{21} s_F R(\omega_{\mathrm{g}} T_s), & l_{31} s_F R(2\omega_{\mathrm{g}} T_s), & \cdots \end{bmatrix} \tag{45}$$

where $l_{11}, l_{21}, l_{31}, \cdots$ and d_{H,N_p} are all the scalar coefficients.

Then, we can construct a Lagrange function L_{NA} for the constrained optimization problem with N_A active control constraints in a similar fashion as in (32) and (37). Further, the optimizer $\boldsymbol{v}_0^*$ is obtained as

$$\begin{aligned}
\boldsymbol{v}_0^* &= \boldsymbol{v}_{\text{unc}} + \lambda_1 \frac{l_{11}}{d_{H,N_p}} \boldsymbol{a} + \lambda_2 \frac{l_{12}}{d_{H,N_p}} s_F R(\omega_{\mathrm{g}} T_s) R(-\omega_{\mathrm{g}} T_s) \boldsymbol{a} \\
&\quad + \lambda_3 \frac{l_{13}}{d_{H,N_p}} s_F R(2\omega_{\mathrm{g}} T_s) R(-2\omega_{\mathrm{g}} T_s) \boldsymbol{a} + \cdots \\
&\quad + \lambda_{NA} \frac{l_{1,N_p}}{d_{H,N_p}} s_F R((N_A - 1)\omega_{\mathrm{g}} T_s) R(-(N_A - 1)\omega_{\mathrm{g}} T_s) \boldsymbol{a} \\
&= \boldsymbol{v}_{\text{unc}} + c_{NA} \boldsymbol{a}
\end{aligned} \tag{46}$$

where c_{NA} is the resulted scalar. We conclude that when N_A control input constraints are active in the general case, the modification term $c_{NA}\boldsymbol{a}$ is also perpendicular to the first voltage constraint.

It is noted that the theoretical analysis above demonstrate that the geometric projection mechanism on obtaining the analytical constrained optimizer is always valid even when the hexagon size varies with the dc-link voltage of BESS. Therefore, the current controller designed in the 2-D problem with fixed V_{dc} can be directly used in the original 3-D problem incorporating the BESS dc-link voltage variations.

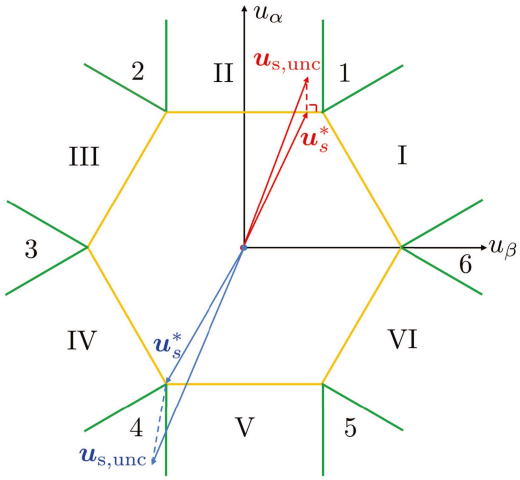

Fig. 4. Illustration of the efficient MPC with analytical solution.

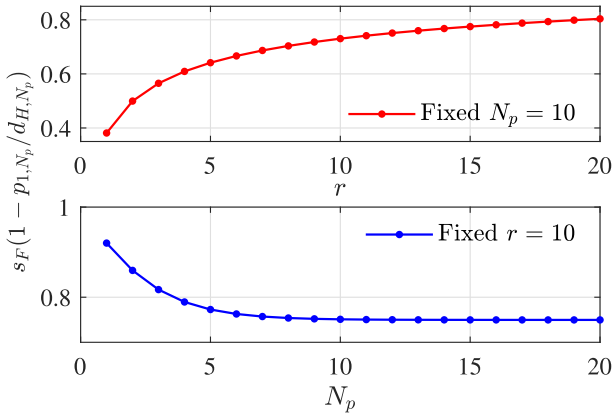

Fig. 5. Illustration of the closed-loop system pole's amplitude $s_F(1 - \frac{p_{1,N_p}}{d_{H,N_p}})$ versus r and N_p. (a) Different control penalty r with fixed predictive horizon $N_p = 10$. (b) Different N_p with fixed $r = 10$.

Moreover, the geometric relationship between the unconstrained and constrained optimal solutions is preserved in both the dq and $\alpha\beta$-frames due to the linear transformation $\boldsymbol{u} = \boldsymbol{v} + \bar{\boldsymbol{u}}$ and the subsequent linear rotation of $\boldsymbol{u}$ to $\boldsymbol{u}_s$ around the origin. Building on this foundation, we propose an APCC for the grid-connected PCS in BESS, offering high computational efficiency.

First, we partition the real voltage plane of the PCS into 12 regions as shown in Fig. 4. Then, for a current tracking error $\boldsymbol{x}_0 = \boldsymbol{i}(t) - \boldsymbol{i}_{\text{ref}}$, we calculate the unconstrained optimal control sequence as $\boldsymbol{V}_{\text{unc}} = -H_{N_p}^{-1} M_{N_p}^T \boldsymbol{x}_0$, with the first control element given by

$$\boldsymbol{v}_{\text{unc}}^0 = \frac{-p_{1,N_p} s_F}{d_{H,Np} s_B} R(-\omega_g T_s - \theta_B)\boldsymbol{x}_0 \triangleq \boldsymbol{K}_{\text{fb}} \boldsymbol{x}_0. \tag{47}$$

Subsequently, the unconstrained solution in the original $\alpha\beta$-frame is obtained as $\boldsymbol{u}_{\text{s,unc}} = R(\theta_g)(\boldsymbol{v}_{\text{unc}}^0 + \bar{\boldsymbol{u}})$. If the unconstrained solution $\boldsymbol{u}_{\text{s,unc}}$ is within the voltage hexagon, then $\boldsymbol{u}_s^* = \boldsymbol{u}_{\text{s,unc}}^0$. If the calculated $\boldsymbol{u}_{\text{s,unc}}$ violates the voltage hexagon and belongs to the region indexed by the Roman numerals $\text{I}, \ldots, \text{V}$, $\boldsymbol{u}_s^*$ is chosen as the projection of $\boldsymbol{u}_{\text{s,unc}}$ to its closest boundary. Otherwise, if $\boldsymbol{u}_{\text{s,unc}}$ locates in the triangular region indexed by Arabic numerals $1, \ldots, 6$, $\boldsymbol{u}_s^*$ is chosen as the closest vertex value. Detailed derivation of $\boldsymbol{v}_{\text{unc}}^0$ is given in Appendix A.

Note that only the gain matrix $\boldsymbol{K}_{\text{fb}}$ is necessary for the computation of $\boldsymbol{v}_{\text{unc}}^0$ based on previous discussions, and it can be calculated offline once the control penalty r and predictive horizon N_p are determined. Therefore, the proposed APCC not only guarantees the analytical solution of MPC with long prediction horizon, but also reduces the online computation dramatically compared with the existing MPC.

Remark 2: In engineering practice, one also uses current and voltage limit circles as system constraints for implementation ease. It can be treated as the generalization of the linear constrained case (23) when N_u and N_i go to infinity. Thus, the theoretical results obtained in the linear constrained case can be readily extended to solve the quadratic one.

D. Stability Analysis and Parameter Tuning Strategy

Subsequently, we analyze the stability of the proposed current controller and then establish parameter tuning strategy. As is common practice, we focus on the convergence dynamics of the tracking error when the system is unconstrained, as the bounded-input and bounded-output stability is inherently guaranteed in the constrained condition. Consequently, the optimal control $\boldsymbol{v}_0^*$ can be treated as a state feedback law, resulting in the closed-loop control system of the grid-connected PCS as

$$\boldsymbol{x}_{k+1} = \boldsymbol{F}\boldsymbol{x}_k + \boldsymbol{B}\boldsymbol{v}_0^* = \left(1 - \frac{p_{1,N_p}}{d_{H,N_p}}\right)\boldsymbol{F}\boldsymbol{x}_k. \tag{48}$$

Then, the poles of the closed-loop system are

$$s_F\left(1 - \frac{p_{1,N_p}}{d_{H,N_p}}\right)(\cos\omega_g T_s \pm j \sin\omega_g T_s). \tag{49}$$

It can be shown that the closed-loop system (49) is always stable for all values of r since the pole's amplitude $s_F(1 - \frac{p_{1,N_p}}{d_{H,Np}})$ is always less than zero.

In addition, as r increases, the magnitude of the pole also increases for a fixed N_p, indicating that a smaller r yields a faster dynamics. Moreover, varying the prediction horizon length N_p results in different H_{N_p}, and consequently, different values of p_{1,N_p} and d_{H,N_p}, which correspond to distinct control laws. Since the fractional $\frac{-p_{1,N_p}}{d_{H,Np}}$ in the control law $\boldsymbol{v}_0^*$ decreases with an increasing prediction horizon N_p when the control penalty r is maintained, a larger N_p can enhance the dynamic response. The relationship between the pole amplitude with respect to the control penalty and the predictive horizon length is also illustrated in Fig. 5.

E. Offset-Free Tracking Performance Design

In practical applications, the dynamic response of the grid-connected PCS is usually disturbed by the unmodeled system dynamics, converter nonlinearities, and grid variations, which can yield degraded control performance, especially the steady-state tracking error. To this end, we combine a disturbance observer

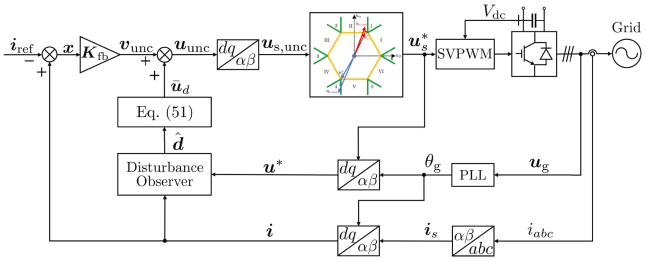

Fig. 6. Structure of the proposed APCC for the PCS of the grid-connected BESS.

with the APCC to reject the lumped disturbance such that the grid-connected PCS can obtain the offset-free current tracking performance. Here, we establish the disturbance observer as

$$\frac{d}{dt}\begin{bmatrix}\hat{\boldsymbol{i}}\\ \hat{\boldsymbol{d}}\end{bmatrix} = \begin{bmatrix}\boldsymbol{A}_c & \boldsymbol{I}\\ \boldsymbol{0} & \boldsymbol{0}\end{bmatrix}\begin{bmatrix}\hat{\boldsymbol{i}}\\ \hat{\boldsymbol{d}}\end{bmatrix} + \begin{bmatrix}\boldsymbol{B}_c\\ \boldsymbol{0}\end{bmatrix}\boldsymbol{u}(t) + \boldsymbol{g}_c + \begin{bmatrix}\boldsymbol{K}_1\\ \boldsymbol{K}_2\end{bmatrix}\boldsymbol{e}$$
$$\boldsymbol{e} = \boldsymbol{i} - \hat{\boldsymbol{i}}. \tag{50}$$

where $\hat{\boldsymbol{d}} = [\hat{d}_1, \hat{d}_2]^T$ is estimation of the lumped disturbance $\boldsymbol{d}$ in the dq-frame, and $\boldsymbol{K}_1$ and $\boldsymbol{K}_2$ are the proper designed 2×2 feedback gain matrices such that the poles of the estimation error dynamics of the disturbance observer (50) are all placed in the left half complex plane.

Then, the steady-state equation of the grid-connected PCS under disturbance becomes $\bar{\boldsymbol{i}} = \boldsymbol{F}\bar{\boldsymbol{i}} + \boldsymbol{B}\bar{\boldsymbol{u}} + \hat{\boldsymbol{d}} + \boldsymbol{g}$. Compared with (13), only the steady-state voltage is shifted to

$$\bar{\boldsymbol{u}}_d = \boldsymbol{B}^{-1}\left[(\boldsymbol{I}-\boldsymbol{F})\bar{\boldsymbol{i}} - \hat{\boldsymbol{d}} - \boldsymbol{g}\right]. \tag{51}$$

Therefore, the analytic solution of the APCC with disturbance compensation can be obtained in a similar manner as in the ideal case discussed in Section IV-C-3. Now, we summarize the detailed procedures of the APCC online implementation in practice as follows:

1) At the time instant t, update the disturbance observer to obtain $\hat{\boldsymbol{i}}$ and $\hat{\boldsymbol{d}}$, and then calculate the steady-state control input $\boldsymbol{u}_d$ and the error signal $\boldsymbol{x}_0 = \boldsymbol{i}(t) - \boldsymbol{i}_{\text{ref}}$.
2) Compute the unconstrained control $\boldsymbol{u}_{\text{unc}} = \boldsymbol{K}_{\text{fb}}\boldsymbol{x}_0 + \boldsymbol{u}_d$.
3) Transform $\boldsymbol{u}_{\text{unc}}$ into $\boldsymbol{u}_{\text{s,unc}}$ in the $\alpha\beta$-frame, and then perform geometric projection strategy shown in Fig. 4 to obtain the optimal control input $\boldsymbol{u}_s^*$.

Detailed control structure of the proposed APCC for the grid-connected PCS is shown in Fig. 6.

V. Simulation and Experimental Results

We now perform simulations and experiments to demonstrate the fast dynamics, low THDs, strong robustness, as well as the high computational efficiency of the proposed APCC for the grid-connected PCS of the BESS.

A. Simulation Results

We first conduct simulation to demonstrate the control performance of the APCC under different constraints. The simulation

TABLE I
Nominal Parameters of the 20-KVA PCS

Variable / Parameter	Actual Value	Normalized Value
Rated power	20 kVA	1.0 p.u.
Rated voltage	$\sqrt{2/3}\cdot$ 380 V	1.0 p.u.
Rated current	$\sqrt{2}\cdot$ 30 A	1.0 p.u.
Maximum current	$1.3\cdot\sqrt{2}\cdot$ 30 A	1.3 p.u.
Rated grid frequency ω_{g}	50 Hz	1.0 p.u.
Rated dc-link voltage V_{dc}	800 V	2.6 p.u.
DC-link capacitance C_{dc}	3.3 mF	7.5 p.u.
Base impedance Z_{b}	7.22 Ω	1.0 p.u.
Filter inductance L_{f}	2.5 mH	0.1 p.u.
Filter resistance R_{f}	0.28 Ω	0.04 p.u.
Switching/Sampling Frequency	10 kHz	200 p.u.

TABLE II
Operating Points in Simulation Investigation

	$\boldsymbol{i}_0$	$\boldsymbol{i}_{\text{ref}}$	Active constraints at $t=0$
a)	(0, 0)	$(0.2, 0)$	$\emptyset$
b)	(0, 0)	$(0.6, 0)$	$\{1\}$
c)	(0, 0)	$(0.55, -0.55)$	$\{6, 12\}$
d)	(0, 0)	$(0.7, 0.15)$	$\{1, 6\}$
e)	(0, 0)	$(0.8, 0.15)$	$\{1, 6, 7\}$
f)	(0, 0)	$(1.0, 0)$	$\{1, 6, 7, 13, 19, 25\}$

results are achieved with accurate system parameters given in Table I. Since the activated constraints are determined by the tracking error between initial state $\boldsymbol{i}_0$ and reference value $\boldsymbol{i}_{\text{ref}}$, as discussed in Section IV, we simulate the dynamic performance of the APCC with different combinations of $\boldsymbol{i}_0$ and $\boldsymbol{i}_{\text{ref}}$ listed in Table II. The corresponding simulation results are illustrated in Fig. 7. Besides the convert current $\boldsymbol{i}(t)$ and voltage $\boldsymbol{u}(t)$ in the dq-frame, the unconstrained control $\boldsymbol{u}_{\text{s,unc}}$ and the constrained optimal control $\boldsymbol{u}_s^*$ are also shown in the $\alpha\beta$-frame for better illustration.

With the reference current set at $\boldsymbol{i}_{\text{ref}} = (0.2, 0)$ p.u., the APCC demonstrates a fast dynamic response to its reference signal in Fig. 7(a). Since the initial tracking error is small, none of the constraints are active in this case, and thus the computed unconstrained control $\boldsymbol{u}_{\text{s,unc}}$ at $t=0$ (denoted by $\circ$) is the same as that of the constrained optimal control $\boldsymbol{u}_s^*$ (denoted by $*$). The convergence dynamics of the APCC satisfies the closed-loop system given in (48).

Subsequently, we increase the reference value to $\boldsymbol{i}_{\text{d,ref}} = 0.3$ p.u. in Fig. 7(b). In this case, the first voltage constraint is active at time instant $t=0$. We observe that the computed unconstrained control $\boldsymbol{u}_{\text{s,unc}}(0)$ indeed violate the voltage, and the projected feasible solution $\boldsymbol{u}_s^*(0)$ is applied to drive the system. For the current control performance, except the transient from $\boldsymbol{i}(0)$ to $\boldsymbol{i}(T_s)$ is limited by the voltage constraint, the convergence dynamics with $t \geq 2T_s$ are the same as the unconstrained case.

In Fig. 7(c), we set $\boldsymbol{i}_{\text{ref}} = (0.55, -0.55)$ p.u, where both the 6th and the 12th constraint in (27) are active at $t=0$. In other words, during the prediction horizon at $t=0$, the control elements at step 1 and 2 in the optimized sequence $\boldsymbol{V}_0^*$ are consecutively active on the sixth edge of the $\alpha\beta$-voltage hexagon

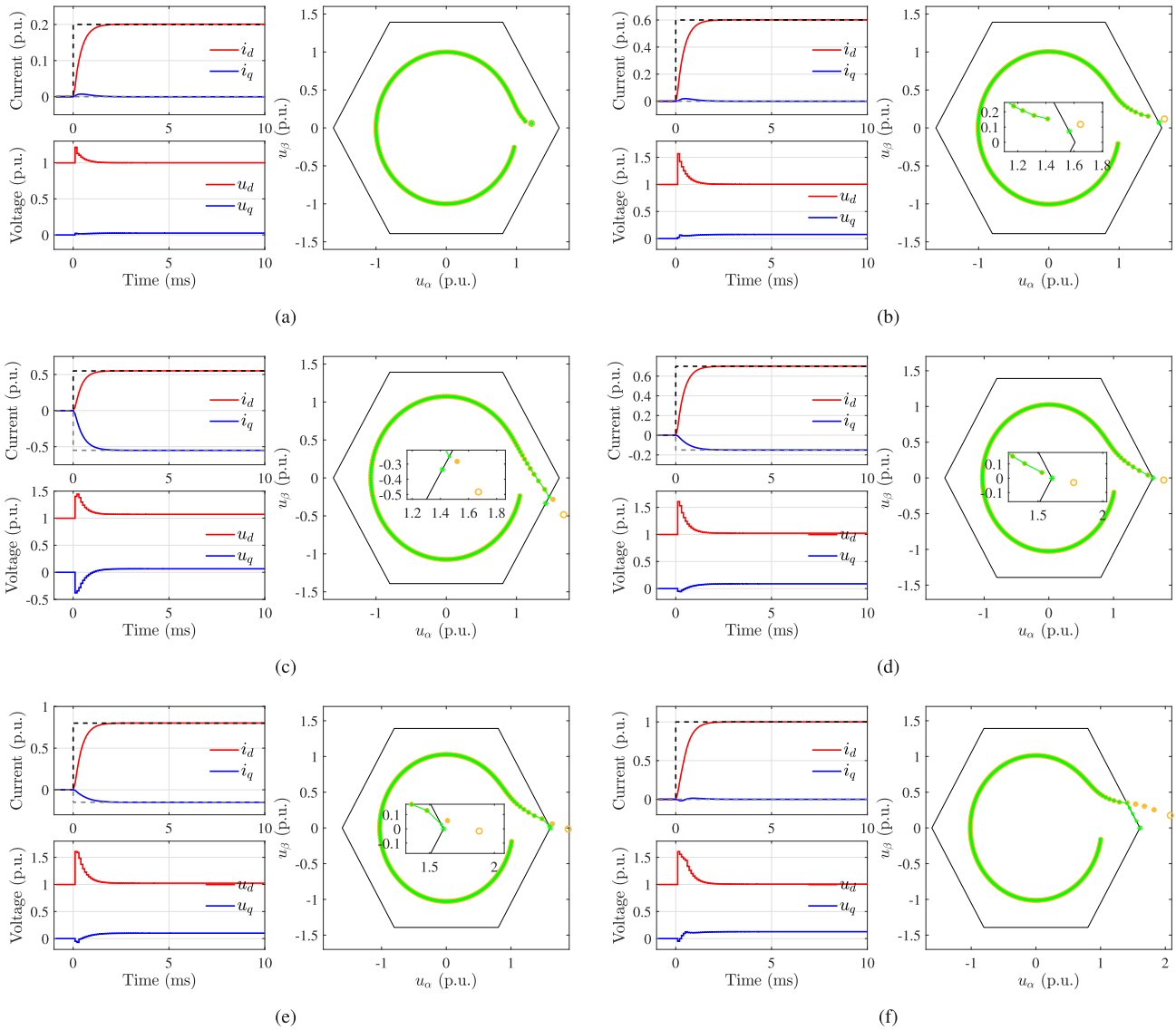

Fig. 7. Simulation results under different constraints at $t = 0$. (a) Unconstrained case. (b) Single active constraint on the edge of the voltage hexagon. (c) Two consecutive active constraints at the same edge. (d) Two simultaneous active constraints at neighboring edges. (e) Three active constraints with the first control in prediction horizon active in the vertex, followed by the second control active in the edge. (f) Rated set-point tracking case involving the aforementioned basic constrained scenarios.

due to the large tracking error. After the closed-system evolves to $\boldsymbol{i}(T_s)$ with the control $\boldsymbol{u}_s^*(0)$, only the 6th constraint remains active and the 12th becomes inactive in the shifted prediction horizon at $t = T_s$, which is similar as that in Fig. 7(b).

Moreover, choosing $\boldsymbol{i}_{\text{ref}} = (0.35, -0.15)$ p.u. in Fig. 7(d), the 1st and the 6th constraint are active, i.e., the control element at step 1 are simultaneously active at the first and sixth edge of the voltage hexagon. It yields the optimal control $\boldsymbol{u}_s^*(0)$ at the vertex at $t = 0$, and the system becomes unconstrained when $t \geq 2T_s$. Furthermore, the 1st, 6th, and 7th constraints are active at $t = 0$ in Fig. 7(e), when we select $\boldsymbol{i}_{\text{ref}} = (0.4, -0.15)$ p.u. As a result, the optimal control $\boldsymbol{u}_s^*(0)$ is firstly applied to the closed-loop system. Then, the system progresses to the state where only the 1st constraint remains active at $t = T_s$, similar to the scenario depicted in Fig. 7(b). Beyond this point, for $t \geq 3T_s$, the system becomes unconstrained again.

Fig. 7(a)–(e) represents modules corresponding to the basic constraint combinations, including the unconstrained case, one single active constraint on the edge of the voltage hexagon, two consecutive active constraints on the same edge, two simultaneous active constraints at the vertex, and an initial active constraint at the vertex followed by one on the edge. Finally, we show the case with $\boldsymbol{i}_0 = (0, 0)$ and $\boldsymbol{i}_{\text{ref}} = (1.0, 0)$ p.u. in Fig. 7(f), where various constraints [No. 1, 6, 7, 13, 19, and 25 in (27)] are active at $t = 0$. The closed-loop system evolves into the unconstrained case after five constrained control periods. In general, the achieved current control performance in Fig. 7 has demonstrated the efficacy of the APCC.

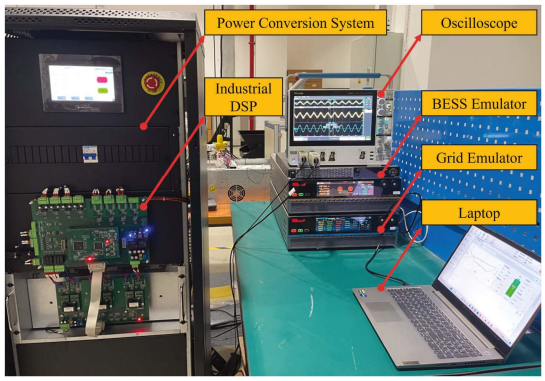

Fig. 8. Experimental platform of the 20-kVA grid-connected PCS equipped with the BESS-Emulator and the Grid-Emulator.

B. Experimental Setup

In the following, we validate the effectiveness of the proposed APCC utilizing a 20-kVA grid-connected BESS experimental platform, as shown in Fig. 8. The experimental platform primarily comprises the BESS-Emulator module, a real PCS, and the grid-emulator module. Particularly, the combination of the BESS and Grid emulators is capable of replicating different kinds of operating conditions. Moreover, a variable impedance cabinet is used in our experiments for emulating different grid strengths. With the measured inputs from the dc-link voltage, converter current, and grid voltage sensors, the proposed APCC is implemented on a real-time digital signal processor (TMS320F28335) control board-one the most commonly used DSPs in the PCS industry. The sampling frequency is set at 10 kHz, which is the same as the switching frequency of the grid-connected PCS. The grid angle is estimated by the mature phase-locked loop (PLL) technique for grid synchronization [31]. Detailed model parameters of the experimental platform are given in Table I, including both the actual and per unit values.

C. Results and Discussions

First, we evaluate the current reference tracking performance of the proposed APCC when the grid-connected BESS operates under normal conditions. Fig. 9 shows the dynamic response of APCC during the charging and discharging switching transient, where the d-axis current reference step up from 0 p.u. to 1.0 p.u, subsequently decreases to -1.0 p.u, and again step back to 0 p.u. The q-axis current reference is set at zero for energy efficiency. From Fig. 9(a), it can be seen that the d-axis current responds quickly to its reference trajectory, and both the dq-axis currents exhibit no static error at steady-state due to the disturbance compensation mechanism.

Next, we demonstrate the effects of the control input penalty r on the control response of the APCC. In Fig. 10(a), the current reference of the grid-connected PCS is changed stepwise from 0 p.u. to 1.0 p.u. The MPC is implemented with the control input penalty r as 3, 5, 10, and 20, respectively, while the prediction horizon is fixed at $N_p = 10$. It can be seen that

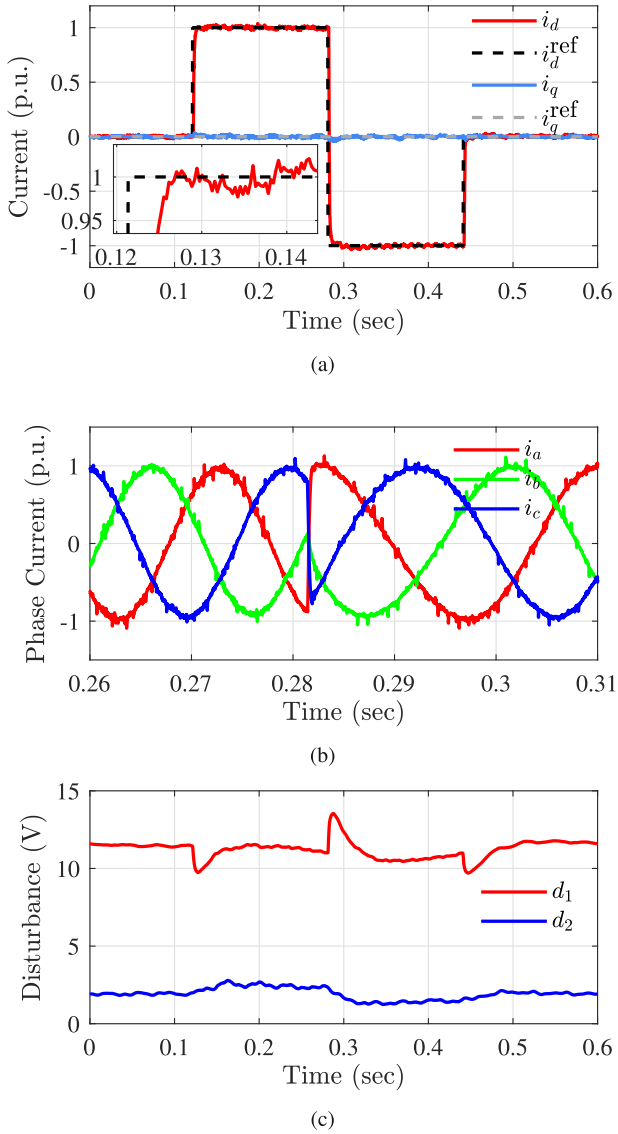

Fig. 9. Typical charging and discharging switching operation of the grid-connected PCS. (a) DQ-axis current tracking performance. (b) Phase currents during the switching transient. (c) Estimated disturbance for offset-free design.

smaller r yields a faster dynamic response, which is identical to the theoretical analysis in Section IV-D. Fig. 10(b) shows the current tracking performance at steady-state, and we observe that the standard deviation (STD) of the d-axis current and the THD of the phase current i_a decreases as r increases, and tend to be more or less the same when $r \geq 5$. In general, excessively small control input penalty can result in large overshoot and even instability problems, which should be avoided in engineering practice.

Subsequently, we investigate the effects of prediction horizon N_p on the current control performance of the proposed controller. As illustrated in Fig. 11(a), the prediction horizon is set at 1, 5, 10, and 20, respectively, whereas the control penalty is maintained at $r = 10$. Fig. 11(a) illustrates that the APCC with longer prediction horizon yields faster dynamic response, while none of the controllers exhibit overshoot under the specified

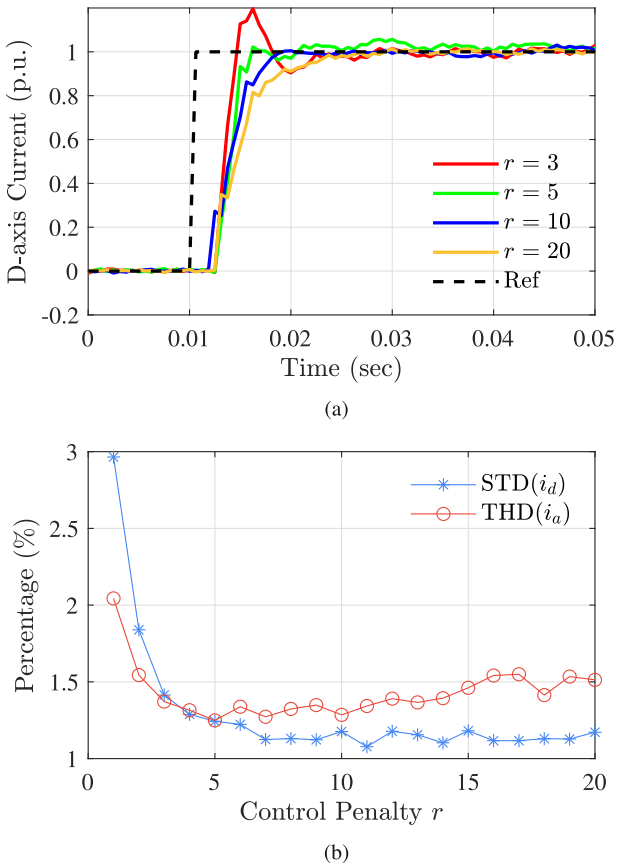

Fig. 10. Current control performance of APCC on different control penalty r. (a) Dynamic response subject to step input. (b) Steady-state tracking performance.

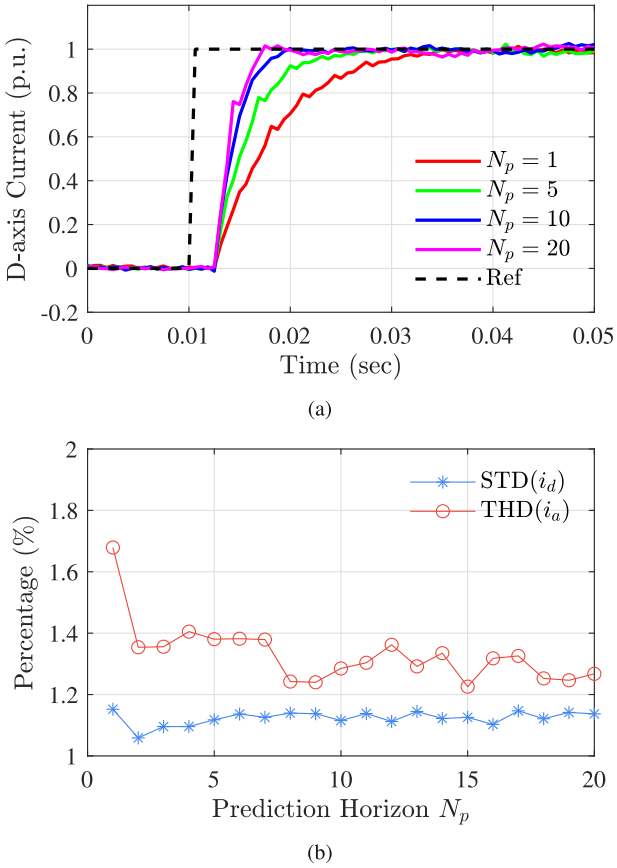

Fig. 11. Current control performance of APCC on different prediction horizon N_p. (a) Dynamic response subject to step input. (b) Steady-state tracking performance.

control penalty setting. From Fig. 11(b), it can be seen that the standard derivation and the THD are marginally affected by the length of the prediction horizon. The experimental results on varying prediction horizon N_p agree well with the theoretical poles shown in Fig. 5.

In the following, we compare the current control performance between the proposed APCC and the widely used optimization based multivariable current controller (OMCC) [9]. As shown in Fig. 12, the current reference trajectory is again changed stepwise from 0 p.u. up to 1.0 p.u. Specifically, in Fig. 12(a), we set the design bandwidth of the OMCC at $\omega_{b0} = 1$ kHz, and tune the control input penalty of the APCC to $r = 10$ to achieve similar steady-state fluctuations for both controllers. It can be observed that the proposed current controller exhibits a faster dynamic response in this case.

To improve the dynamic response of the OMCC, we increased its design bandwidth to $2\omega_{b0}$ in Fig. 12(b), while maintained the control penalty of APCC at $r = 10$. We observe that the dynamic responses of both controllers are almost the same fast, but the OMCC method shows significant overshoot in both the step-up and step-down transients. Moreover, the steady-state current achieved by the OMCC exhibits larger fluctuation compared to the proposed predictive current controller.

To further elucidate the fast dynamics of the APCC at windup operating condition, we compare the proposed APCC with the conventional decoupled-PI method [7], and the latter one usually encounter inadequate antiwindup performance in industry due to its integral mechanism. In Fig. 13, we removed the current protection mechanism of the grid-connected PCS and reduced the voltage hexagon size in software on purpose. The d-axis current is controlled to follow the 1.5 p.u. reference signal at a under-voltage condition, and then to step back to 0 p.u. Fig. 13 shows that the achieved currents of the both controllers slowly exceed the maximally allowed limit and gradually enter the saturation since the dc-link voltage of the BESS is fully utilized at the specified under-voltage condition setting. Moreover, when the command signal returns to 0 p.u., the APCC algorithm responds much faster than the decoupled PI current controller.

Now, we show the offset-free tracking performance of the APCC under parameter uncertainties. The tracking performance of the current controller was again evaluated subjected to the step input. In Fig. 14(a), the APCC was firstly implemented with accurate inductance parameter value, then with 50%, 80%, 120%, and 150% of the nominal value, respectively. From Fig. 14(a), we observe that smaller inductance value yields faster dynamic response. This observation aligns with the closed loop system (48), since smaller L_f corresponds to smaller s_F, i.e., smaller norm of the poles given in (49), and thus results in faster convergence.

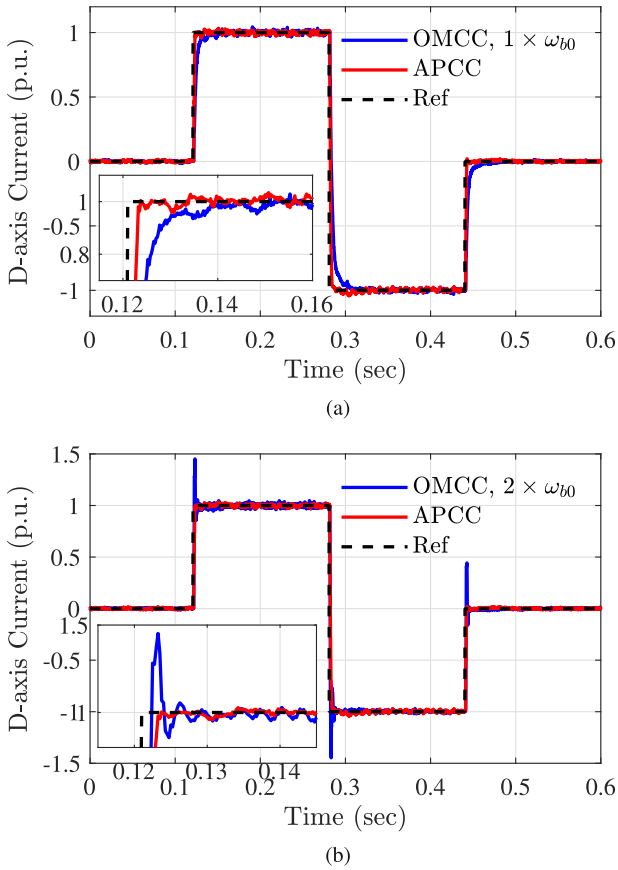

Fig. 12. Current control performance comparison between the proposed APCC and the optimization based multi-variable current controller (OMCC) [9]. (a) OMCC with the design bandwidth set at 1 kHz. (b) OMCC with the design bandwidth set at 2 kHz.

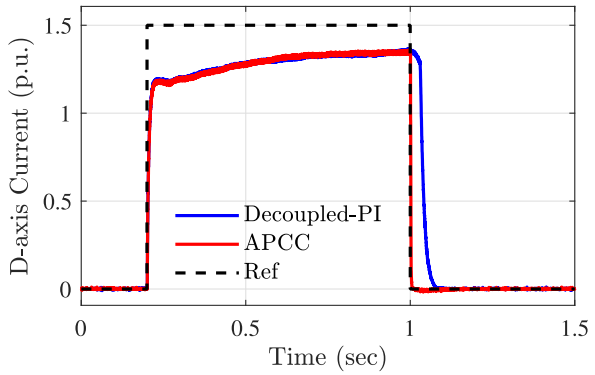

Fig. 13. Comparison between the proposed APCC and the decoupled-PI current controller [7] on the antiwindup performance.

Similar experiments on the induced resistance were conducted in Fig. 14(b), where the experimental values of the resistance is chosen as the 50%, 80%, 120%, and 200% of the nominal one, respectively. It can be seen that the dynamic responses with inaccurate resistance values are slightly different from the ones with accurate value. Due to the offset-free design, all these controllers in Fig. 14 demonstrate offset-free tracking performance in steady-state even under model parameter uncertainties.

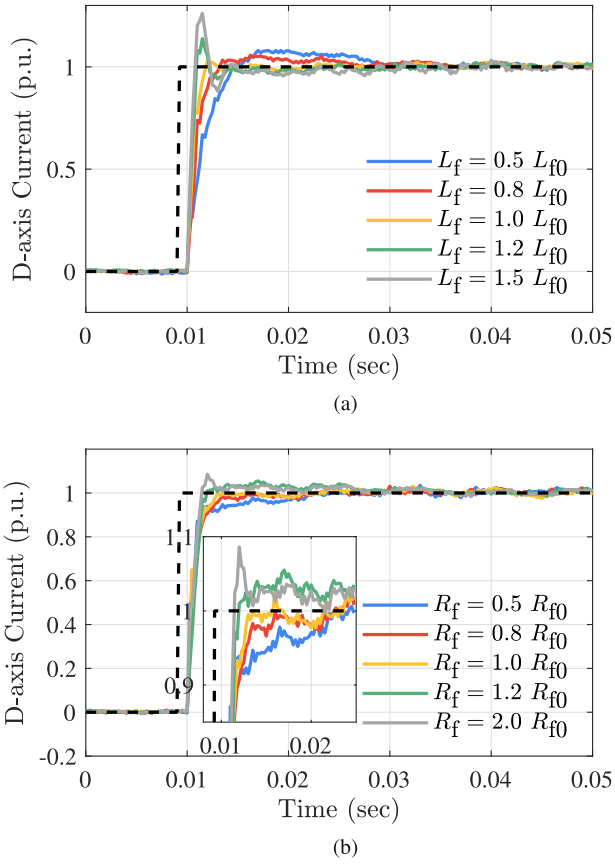

Fig. 14. Step current reference tracking performance of the APCC under model parameter uncertainties. (a) Variations on the filter inductance L_f. (b) Variations on the induced filter resistance R_f.

In Fig. 15, we evaluate the robustness of the proposed analytic predictive current controller against the grid variations. Specifically, the d-axis current of the grid-connected PCS is controlled at 1.0 p.u. at first. Then, the grid frequency is stepwise changed by the Grid-Emulator from the rated 50 Hz to the 45 Hz at 1.25 s to emulate the practical scenarios particularly those involving high-loaded grids experiencing frequency drops. It can be seen that the output current of the PCS can maintain at 1.0 p.u. throughout the frequency variation. Moreover, the norm of the d-axis ripple current becomes smaller due to the frequency drop. Similar robust experimental outcomes of the APCC are observed under grid voltage amplitude variation.

In the following, we compare the robust tracking performance of the proposed APCC with the well-established robust VCC [14], [15] under different grid strength in Fig. 16. The grid inductance L_g and the filter inductance L_f forms the total inductance $L = L_g + L_f$ of the grid-connected system, and the short-circuit ratio (SCR) is defined by the inverse p.u. value of L. Two different values of L_g are considered in our experiments, corresponding to the strong grid condition ($L = 0.15$ p.u., SCR $= 6.7$) and the weak grid condition ($L = 0.5$ p.u., SCR $= 2$), respectively.

As depicted in Fig. 16, the d-axis current is regulated to track a three-stage step-wise reference signal while the q-axis current is

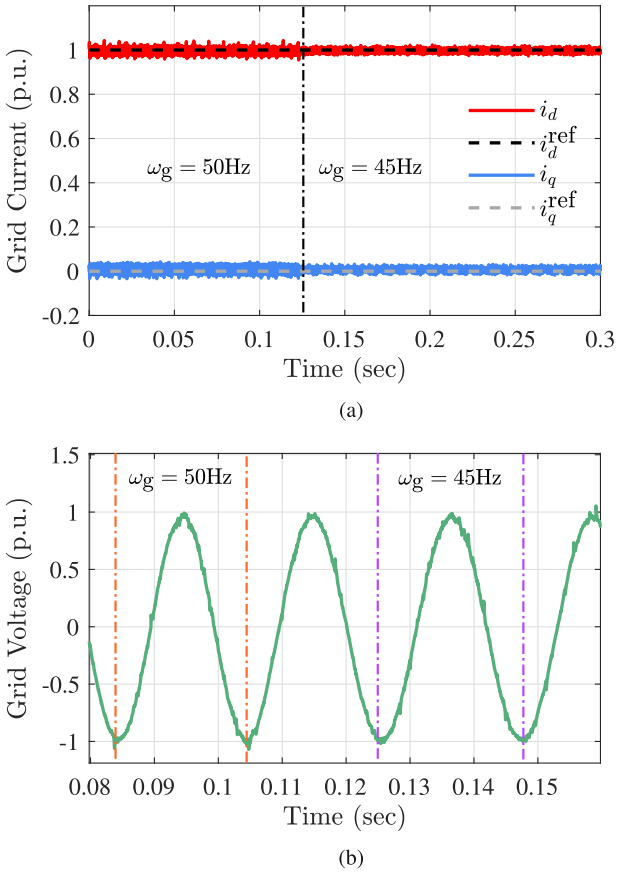

Fig. 15. Current reference tracking performance of the APCC under grid frequency variations. (a) d-axis currents controlled at 1.0 p.u. (b) Grid frequency varies from 1.0 p.u. to 0.9 p.u.

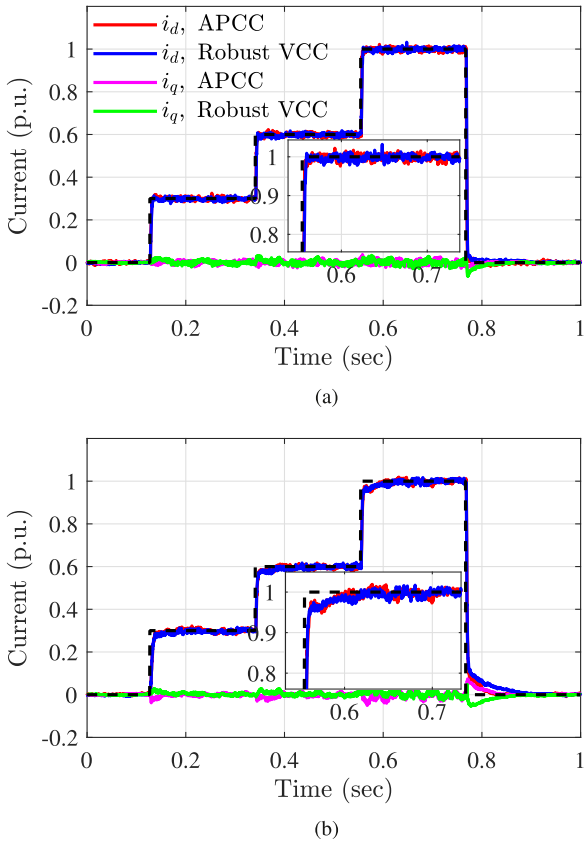

Fig. 16. Robustness comparison between the proposed APCC and the Robust VCC under different grid strength. (a) In strong grid condition ($L = 0.15$ p.u., SCR $= 6.7$). (b) In weak grid condition ($L = 0.5$ p.u., SCR $= 2$).

controlled at 0 p.u. The estimated inductance parameter used in both controllers is fixed at $\hat{L} = 0.2$ p.u. In the strong grid conditions as shown in Fig. 16(a), we tune the control penalty $r = 20$ such that the APCC achieves a dynamic response comparable to that of the robust VCC. With the same parameter setting, Fig. 16(b) illustrates the controller performance in weak grid conditions. Although both the APCC and the robust VCC exhibit slower dynamics under these conditions, they show offset-free tracking performance at steady state. It demonstrates that the proposed APCC can achieve robustness to grid strength similar to that of the robust VCC, but with the advantage of requiring only a single tuning parameter r.

Subsequently, Fig. 17 compares the robustness of the APCC against uncertainties in the filter resistance R_f with the robust VCC, since the parameter value $\hat{R}$ used in controller also includes the converter losses and is typically determined empirically, as discussed in [15]. In strong grid conditions (SCR $= 6.7$), the current tracking performance of both controllers under the over-estimated $\hat{R} = 0.08$ p.u. and the under-estimated $\hat{R} = 0.02$ p.u. is presented in Fig. 17(a) and (b), respectively. The results indicate that variations on $\hat{R}$ reflect only marginal effect on the dynamic response of either the APCC or the robust VCC, and both controllers demonstrate efficacy in eliminating quasi-constant model uncertainties.

TABLE III
EXECUTION TIME OF THE APCC-BASED SOFTWARE ON DSP

Functional module	Execution time (μs)
Control law calculation	2.2
Geometric projection	1.3
Disturbance observer	3.0
PLL	2.8
SVPWM	1.9
Other (ADC, coordinate transformation, trip, etc.)	10.0
Total	21.2

Last, we demonstrate the computational efficiency of the proposed APCC. Distinguished from the conventional MPC, which requires the computationally intensive online solution of complex algebraic differential equations (ADE), the implementation procedures of the APCC, as discussed in Section IV-E, involve only basic arithmetic operations such as addition and multiplication. This significantly reduces the computational burden, making the APCC a highly efficient method. In addition, the detailed execution times of the APCC-based software, implemented on a normal industrial DSP (TMS320F28335), are presented component-wise in Table III.

Moreover, Table IV presents a comparison of the computational times for the proposed APCC, the Explicit MPC [29], and the MATLAB MPC Toolbox [32], all evaluated on the same

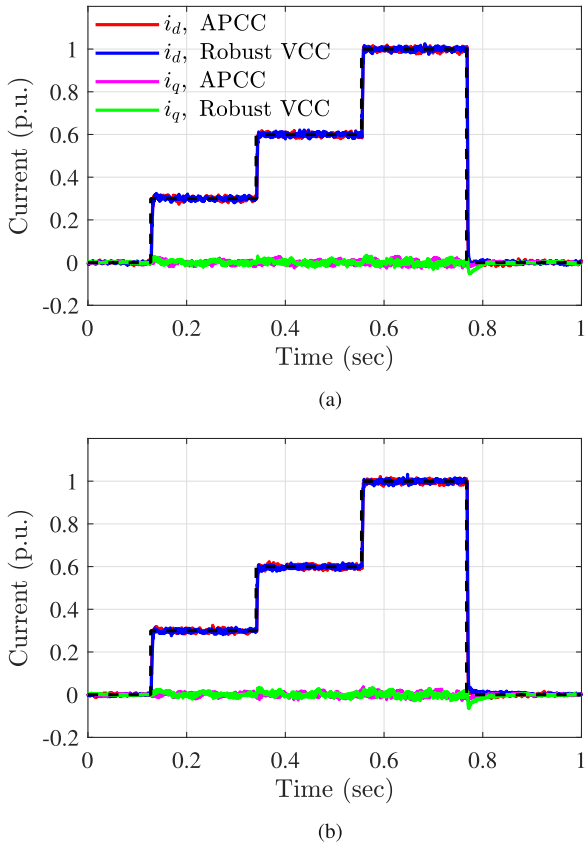

Fig. 17. Robustness comparison between the proposed APCC and robust VCC against resistance uncertainties. (a) Over-estimated resistance case with $\hat{R} = 0.08$ p.u. (b) Under-estimated resistance case with $\hat{R} = 0.02$ p.u.

TABLE IV
COMPARISON OF COMPUTATIONAL TIMES UNDER DIFFERENT NUMBERS OF CRITICAL REGIONS (μs)

No. of critical regions	1	7	13	19	25
Proposed APCC	3.45	3.55	3.50	3.45	3.50
Explicit MPC [29]	3.95	4.45	7.25	10.05	24.95
Matlab MPC Toolbox [32]	20.05	29.95	50.25	80.10	120.05

DSP under different numbers of critical regions, i.e., active constraints, resulted by the varying dc-link voltage. Only the execution time of the core program responsible for solving the constrained finite time optimal control problem is considered in Table IV. Note that the computational times of the APCC method remain relatively consistent across all cases, while the times for the Explicit MPC and MATLAB MPC Toolbox increase with the number of critical regions.

VI. CONCLUSION

In this article, we proposed an APCC for the grid-connected PCS in BESS, to address the critical requirements for fast dynamic response, strong robustness and high computational efficiency. The 3-D current reference tracking problem, accounting for the BESS dc-link voltage variation, was formulated as a multiparametric quadratic problem. We clarified that the 3-D spatial critical regions in this problem are a direct extension of the 2-D planar critical regions, where the size and orientation of the regular hexagon are determined solely by the dc-link voltage. Both unconstrained and constrained optimal solutions were explicitly derived for the optimal control problem, and demonstrated their precise geometric projection relationship in the voltage plane. Leveraging this relationship, the analytic solution of the APCC was achieved with significantly lower computational cost than conventional MPC methods, making the APCC with a long prediction horizon feasible for cost-sensitive industrial applications. In addition, a disturbance observer was combined with the APCC to ensure offset-free tracking performance under mismatches. Simulation and experimental results validated the promising control performance of the APCC compared to the existing well-known current controllers, along with its strong robustness against parameter uncertainties and grid variations.

APPENDIX A
DERIVATION OF OPTIMAL CONTROL IN GENERAL N_p CASE

Now, we provide the detailed derivation on the unconstrained optimal control law $\boldsymbol{v}_{\text{unc}}^0$ for general N_p prediction horizon. In this case, the optimized control sequence $\boldsymbol{V}_{\text{unc}}$ is obtained as

$$\begin{aligned}
&\boldsymbol{V}_{\text{unc}} = -H_{N_p}^{-1} M_{N_p}^T \boldsymbol{x}_0 \\
&= -H_{N_p}^{-1}(H_{N_p} - r\boldsymbol{I})\mathcal{S}_u^{-1}\mathcal{S}_x\boldsymbol{x}_0 = -(\boldsymbol{I} - rH_{N_p}^{-1})\mathcal{S}_u^{-1}\mathcal{S}_x\boldsymbol{x}_0 \\
&= (rH_{N_p}^{-1} - \boldsymbol{I}) \begin{bmatrix} \boldsymbol{B}^{-1} & & & \\ -\boldsymbol{B}^{-1}\boldsymbol{F} & \boldsymbol{B}^{-1} & & \\ & \ddots & \ddots & \\ & & -\boldsymbol{B}^{-1}\boldsymbol{F} & \boldsymbol{B}^{-1} \end{bmatrix} \\
&\quad \times \begin{bmatrix} \boldsymbol{F} \\ \boldsymbol{F}^2 \\ \vdots \\ \boldsymbol{F}^{N_p} \end{bmatrix} \boldsymbol{x}_0 \\
&= (rH_{N_p}^{-1} - \boldsymbol{I}) \begin{bmatrix} \boldsymbol{B}^{-1}\boldsymbol{F} \\ \boldsymbol{0} \\ \vdots \\ \boldsymbol{0} \end{bmatrix} \boldsymbol{x}_0 = \frac{-1}{d_{H,N_p}} \begin{bmatrix} p_{1,N_p}\boldsymbol{F} \\ p_{2,N_p}\boldsymbol{F}^2 \\ \vdots \\ p_{N_p,N_p}\boldsymbol{F}^{N_p} \end{bmatrix} \boldsymbol{B}^{-1}\boldsymbol{x}_0
\end{aligned} \tag{52}$$

where $p_{1,N_p} = d_{H,N_p} - rl_{11}$, $p_{2,N_p} = -rl_{21}$, $\ldots$, $p_{N_p,N_p} = -rl_{N_p,1}$, and l_{ij} is the element of $H_{N_p}^{-1}$ given in (43).

Then, we can obtain the first control element of $\boldsymbol{V}_{\text{unc}}^*$ as follows:

$$\boldsymbol{v}_{\text{unc}}^0 = \frac{-p_{1,N_p}}{d_{H,Np}}\boldsymbol{F}\boldsymbol{B}^{-1}\boldsymbol{x}_0 = \frac{-p_{1,N_p}s_F}{d_{H,Np}s_B}R(-\omega_g T_s - \theta_B)\boldsymbol{x}_0 \tag{53}$$

and $\boldsymbol{v}_{\text{unc}}^0$ function as the foundation for generating the optimal control $\boldsymbol{v}_0^*$ through the proposed analytic geometric projection method.

REFERENCES

[1] F. Blaabjerg, Y. Yang, K. A. Kim, and J. Rodriguez, "Power electronics technology for large-scale renewable energy generation," *Proc. IEEE*, vol. 111, no. 4, pp. 335–355, Apr. 2023.

[2] F. Blaabjerg, R. Teodorescu, M. Liserre, and A. V. Timbus, "Overview of control and grid synchronization for distributed power generation systems," *IEEE Trans. Ind. Electron.*, vol. 53, no. 5, pp. 1398–1409, Oct. 2006.

[3] V. Pirsto, J. Kukkola, and M. Hinkkanen, "Multifunctional cascade control of voltage-source converters equipped with an LC filter," *IEEE Trans. Ind. Electron.*, vol. 69, no. 3, pp. 2610–2620, Mar. 2022.

[4] A. Timbus, M. Liserre, R. Teodorescu, P. Rodriguez, and F. Blaabjerg, "Evaluation of current controllers for distributed power generation systems," *IEEE Trans. Power Electron.*, vol. 24, no. 3, pp. 654–664, Mar. 2009.

[5] E. Twining and D. G. Holmes, "Grid current regulation of a three-phase voltage source inverter with an LCL input filter," *IEEE Trans. Power Electron.*, vol. 18, no. 3, pp. 888–895, May 2003.

[6] M. Liserre, R. Teodorescu, and F. Blaabjerg, "Multiple harmonics control for three-phase grid converter systems with the use of PI-RES current controller in a rotating frame," *IEEE Trans. Power Electron.*, vol. 21, no. 3, pp. 836–841, May 2006.

[7] J. Kukkola, M. Hinkkanen, and K. Zenger, "Observer-based state-space current controller for a grid converter equipped with an LCL filter: Analytical method for direct discrete-time design," *IEEE Trans. Ind. Appl*, vol. 51, no. 5, pp. 4079–4090, Sep./Oct. 2015.

[8] B. Bahrani, S. Kenzelmann, and A. Rufer, "Multivariable-pi-based *dq* current control of voltage source converters with superior axis decoupling capability," *IEEE Trans. Ind. Electron.*, vol. 58, no. 7, pp. 3016–3026, Jul. 2011.

[9] B. Bahrani, A. Karimi, B. Rey, and A. Rufer, "Decoupled DQ-current control of grid-tied voltage source converters using nonparametric models," *IEEE Trans. Ind. Electron.*, vol. 60, no. 4, pp. 1356–1366, Apr. 2013.

[10] D. N. Zmood and D. G. Holmes, "Stationary frame current regulation of PWM inverters with zero steady-state error," *IEEE Trans. Power Electron.*, vol. 18, no. 3, pp. 814–822, May 2003.

[11] R. Teodorescu, F. Blaabjerg, M. Liserre, and P. C. Loh, "Proportional-resonant controllers and filters for grid-connected voltage-source converters," *IEE Proc.-Electric Power Appl.*, vol. 153, no. 5, pp. 750–762, 2006.

[12] T. Ye, N. Dai, C.-S. Lam, M.-C. Wong, and J. M. Guerrero, "Analysis, design, and implementation of a quasi-proportional-resonant controller for a multifunctional capacitive-coupling grid-connected inverter," *IEEE Trans. Ind. Appl.*, vol. 52, no. 5, pp. 4269–4280, Sep./Oct. 2016.

[13] D. Chen, J. Zhang, and Z. Qian, "An improved repetitive control scheme for grid-connected inverter with frequency-adaptive capability," *IEEE Trans. Ind. Electron.*, vol. 60, no. 2, pp. 814–823, Feb. 2013.

[14] L. Harnefors, "Voltage source converter (VSC) control system with active damping," US. Patent 10,170,914, Jan. 1 2019.

[15] L. Harnefors, J. Kukkola, M. Routimo, M. Hinkkanen, and X. Wang, "A universal controller for grid-connected voltage-source converters," *IEEE Trans. Emerg. Sel. Topics Power Electron.*, vol. 9, no. 5, pp. 5761–5770, Oct. 2021.

[16] I. J. Gabe, V. F. Montagner, and H. Pinheiro, "Design and implementation of a robust current controller for VSI connected to the grid through an LCL filter," *IEEE Trans. Power Electron.*, vol. 24, no. 6, pp. 1444–1452, Jun. 2009.

[17] X. Huang et al., "Robust current control of grid-tied inverters for renewable energy integration under non-ideal grid conditions," *IEEE Trans. Sustain. Energy*, vol. 11, no. 1, pp. 477–488, Jan. 2020.

[18] C. R. D. Osório, G. G. Koch, H. Pinheiro, R. C. Oliveira, and V. F. Montagner, "Robust current control of grid-tied inverters affected by LCL filter soft-saturation," *IEEE Trans. Ind. Electron.*, vol. 67, no. 8, pp. 6550–6561, Aug. 2020.

[19] P. Karamanakos, E. Liegmann, T. Geyer, and R. Kennel, "Model predictive control of power electronic systems: Methods, results, and challenges," *IEEE Open J. Ind. Appl.*, vol. 1, pp. 95–114, 2020.

[20] F. Borrelli, A. Bemporad, and M. Morari, *Predictive Control for Linear and Hybrid Systems*. Cambridge, MA, USA: Cambridge Univ. Press, 2017.

[21] M. Preindl, E. Schaltz, and P. Thogersen, "Switching frequency reduction using model predictive direct current control for high-power voltage source inverters," *IEEE Trans. Ind. Electron.*, vol. 58, no. 7, pp. 2826–2835, Jul. 2011.

[22] T. Geyer, G. Papafotiou, and M. Morari, "Model predictive direct torque control—Part I: Concept, algorithm, and analysis," *IEEE Trans. Ind. Electron.*, vol. 56, no. 6, pp. 1894–1905, Jun. 2009.

[23] P. Karamanakos, T. Geyer, and R. P. Aguilera, "Long-horizon direct model predictive control: Modified sphere decoding for transient operation," *IEEE Trans. Ind. Appl.*, vol. 54, no. 6, pp. 6060–6070, Nov./Dec. 2018.

[24] A. Linder and R. Kennel, "Model predictive control for electrical drives," in *Proc. IEEE 36th Power Electron. Specialists Conf.*, 2005, pp. 1793–1799.

[25] S. Mariéthoz and M. Morari, "Explicit model-predictive control of a PWM inverter with an LCL filter," *IEEE Trans. Ind. Electron.*, vol. 56, no. 2, pp. 389–399, Feb. 2009.

[26] A. Bemporad, "Explicit model predictive control," in *Encyclopedia of Systems and Control*. Berlin, Germany: Springer, pp. 744–751, 2021.

[27] A. Bemporad, F. Borrelli, and M. Morari, "Model predictive control based on linear programming the explicit solution," *IEEE Trans. Autom. Control.*, vol. 47, no. 12, pp. 1974–1985, Dec. 2002.

[28] A. Bemporad, M. Morari, V. Dua, and E. N. Pistikopoulos, "The explicit linear quadratic regulator for constrained systems," *Automatica*, vol. 38, no. 1, pp. 3–20, 2002.

[29] M. Herceg, M. Kvasnica, C. N. Jones, and M. Morari, "Multi-parametric toolbox 3.0," in *Proc. Eur. control Conf.*, 2013, pp. 502–510.

[30] H. K. Khalil, *Control of Nonlinear Systems*. Prentice Hall, New York, NY, USA, 2002.

[31] S.-K. Chung, "Phase-locked loop for grid-connected three-phase power conversion systems," *IEE Proc.-Electric Power Appl.*, vol. 147, no. 3, pp. 213–219, 2000.

[32] Y. Chen, M. Bruschetta, E. Picotti, and A. Beghi, "Matmpc-a MATLAB based toolbox for real-time nonlinear model predictive control," in *Proc. 18th Eur. Control Conf.*, 2019, pp. 3365–3370.

Mingming Zhang received the B.S. degree in mechanical engineering from East China University of Science and Technology, Shanghai, China, in 2015, the M.S. degree in mechanical engineering and the Ph.D degree in control science and engineering from Shanghai Jiao Tong University, Shanghai, China, in 2019 and 2022, respectively.

He is currently a postdoctoral Researcher with the Global Institute of Future Technology, Shanghai Jiao Tong University. His research interests include grid-connected converter control and motion control.

Mian Li (Member, IEEE) received the B.E. and M.S. degrees in automation from Tsinghua University, Beijing, China, in 1999 and 2001, respectively, and the Ph.D. degree from the Department of Mechanical Engineering, University of Maryland at College Park, College Park, MD, USA, in 2007, with the Best Dissertation Award.

He is currently a Tenured Professor and an Assistant Dean of the Global Institute of Future Technologies in Shanghai Jiao Tong University. His research interests include design automation, data analysis methods, and machine learning, in addition to robust/reliability-based multidisciplinary design optimization.

Jun Zhang (Senior Member, IEEE) received the B.S. degree in automatic control from Shanghai Jiao Tong University, Shanghai, China, in 1993, and the M.S. and Ph.D. degrees in electrical engineering from the University of California at Berkeley, CA, USA, in 1999 and 2003, respectively.

After that he worked at several high tech firms in the Silicon Valley. He is currently a Professor with the UMich-SJTU Joint Institute, Shanghai Jiao Tong University. His research interests include motion control and complex system control.